



# Photocatalysis activation of peroxydisulfate over the supported Fe<sub>3</sub>O<sub>4</sub> catalyst derived from MIL-88A(Fe) for efficient tetracycline hydrochloride degradation

Xiu-Wu Zhang, Fei Wang, Chong-Chen Wang<sup>\*</sup>, Peng Wang, Huifen Fu, Chen Zhao

Beijing Key Laboratory of Functional Materials for Building Structure and Environment Remediation, School of Environment and Energy Engineering, Beijing University of Civil Engineering and Architecture, Beijing 100044, China

## ARTICLE INFO

### Keywords:

Fe<sub>3</sub>O<sub>4</sub>  
MIL-88A  
Persulfate activation  
Tetracycline hydrochloride  
Immobilization

## ABSTRACT

Within this paper, the MIL-88A(Fe) particles were immobilized onto the commercial porous block substrate (PBS) to form MIL-88A/PBS via a simple room-temperature synthesis method, which was further calcined at high temperature like 400 °C, 500 °C, 600 °C and 700 °C to obtain Fe<sub>3</sub>O<sub>4</sub>@PBS (M-Fe<sub>3</sub>O<sub>4</sub>-T@PBS). Upon the irradiation of white light, the peroxydisulfate (PDS) was activated over the as-obtained M-Fe<sub>3</sub>O<sub>4</sub>-T@PBS to accomplish tetracycline hydrochloride (TC) degradation in the simulated wastewater. The results revealed that 97.5% and 92.8% TC with the initial concentration of 10 mg L<sup>-1</sup> could be degraded within 40.0 min via PDS activation over the optimum catalyst M-Fe<sub>3</sub>O<sub>4</sub>-600@PBS under white light and real sunlight irradiation, respectively. The influence factors including PDS dosage, pH values and co-existing ions toward the degradation performance of M-Fe<sub>3</sub>O<sub>4</sub>-600@PBS were investigated. Importantly, M-Fe<sub>3</sub>O<sub>4</sub>-600@PBS could accomplish extremely simple recyclability and excellent reusability, affording high oxidative degradation even after 30 successive recycles. The possible degradation mechanism explored via different methods like active species capture experiments, electron spin resonance (ESR) determination as well as the corresponding electrochemical analyses. Furthermore, the possible pathways of TC degradation were depicted based on Liquid Chromatography-Mass spectrometry (LC-MS) technology, in which the toxicity of the intermediates decreased based on the quantitative structure-activity relationship (QSAR) evaluation. This work revealed that the immobilized Fe-based MOFs derivatives catalysts possessed great potential in real and large-scale wastewater remediation.

## 1. Introduction

Antibiotics are considered to be persistent and refractory trace pollutants in water environments. Most antibiotics cannot be completely absorbed and metabolized by human and animal bodies, resulting in a large number of antibiotics being released into the environment through urine and feces [1,2]. The abuse of antibiotics leads to their excessive discharge into the natural water environment, which directly destroys the aquatic ecology and threatens human health [3,4]. Also, the large-scale influx of antibiotics into the water environments can cause the further evolution and wide spread of antibiotic-resistant bacteria (ARB) along with antibiotic resistance genes (ARGs), which may lead to a major public health security crisis [5]. Among many antibiotics, tetracycline antibiotics (TCs) are commonly used in fishery, plantation and animal husbandry, and are even widely added to feed as growth

promoters [6]. Most of the TCs are discharged into the water environment, which may lead to enhanced microbial resistance and endanger the safety of ecology and humans [7,8]. Therefore, the treatment of wastewater containing TCs is essential and urgent.

In recent years, various methods of removing TCs in water bodies have been studied, including adsorption [9], biotechnology [10], membrane separation [11,12] and advanced oxidation processes (AOPs) [13–15]. AOPs can effectively attack the molecular structure of most organic pollutants, which might completely mineralize them into carbon dioxide and water without the discharge of secondary pollutants [16,17]. AOPs was considered to be one of the most promising sewage treatment technologies, despite of that there was still much to be improved in terms of catalyst improvement and design of operating parameters, [18–20]. Being compared with the counterpart AOP technologies based on hydroxyl radicals (•OH), sulfate radicals (SO<sub>4</sub><sup>•-</sup>)

<sup>\*</sup> Corresponding author.

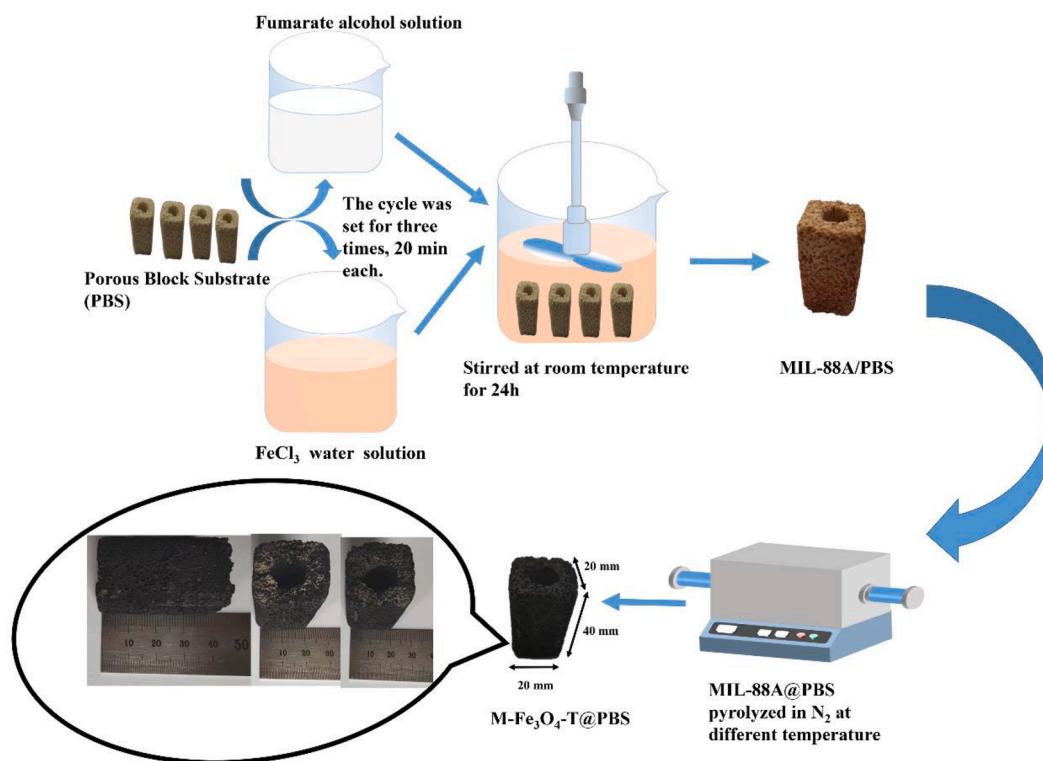
E-mail addresses: [wangchongchen@bucea.edu.cn](mailto:wangchongchen@bucea.edu.cn), [chongchenwang@126.com](mailto:chongchenwang@126.com) (C.-C. Wang).

<https://doi.org/10.1016/j.cej.2021.131927>

Received 11 June 2021; Received in revised form 3 August 2021; Accepted 15 August 2021

Available online 21 August 2021

1385-8947/© 2021 Elsevier B.V. All rights reserved.



**Scheme 1.** Schematic illustration of  $M\text{-Fe}_3\text{O}_4\text{-T@PBS}$  production via the calcination of MIL-88A/PBS.

based-advanced oxidation processes (SR-AOPs) had attracted increasing attentions, due to the higher redox potential (2.5–3.1 V vs. SHE), longer half-life (30–40  $\mu\text{s}$ ) in solution and wider pH adaptability (2.0–11.0) [18,21]. Particularly, the peroxydisulfate (PDS,  $\text{S}_2\text{O}_8^{2-}$ ) demonstrated some advantages like stable under external environment and low-cost. Generally, PDS can be activated to produce  $\text{SO}_4^{\bullet-}$  radicals by various methods like transition metals/oxides [22,23], ionizing radiation [24], heat [25], alkaline solutions [26], sonication [27], carbonaceous materials [28], UV or visible light [29], and photocatalysis [30]. It needs to be pointed out that photocatalysis activation of peroxydisulfate has attracted extensive attentions due to its great potential to produce  $\text{SO}_4^{\bullet-}$  radicals with the presence of catalysts under sustainable solar energy [29]. From these points, it was essential to develop some effective catalysts to enhance the photocatalysis activation SR-AOPs.

Metal-organic frameworks (MOFs) are produced by the coordination reaction between metal ions/clusters and organic ligands, with huge surface area and crystal structure [31,32] are widely used in the environmental remediation processes including photocatalysis [33–38], Fenton-like catalysis [30,39] and persulfate activation [40]. Fe-based MOFs, especially MIL-88A(Fe) is friendly to the environment and exhibits excellent thermal & chemical stability, as well as outstanding light responsive activity (the detailed descriptions for different Fe-MOFs like MIL-53(Fe), MIL-88A(Fe), MIL-88B(Fe), MIL-100(Fe), MIL-101(Fe) were provided in ESI, Table S1). Nowadays, more and more Fe-MOFs were adopted as precursors and templates to fabricate different inorganic derivatives for accomplishing boosted performances [41–43]. In particular, Fe-based inorganic catalyst containing Fe(II)/Fe(III) can activate PDS/PMS through the catalysis cycle to achieve efficient organic pollutants degradation [44,45]. Wang et al. synthesized CoFe/NC porous hybrid nanorods from a bismetal-organic framework to achieve outstanding persulfate activation for bisphenol A (BPA) degradation [46]. Liu et al. prepared  $\text{NH}_2$ -group incorporation Fe@porous carbon derived from MIL-53(Fe) to accomplish the enhanced catalytic activity and stability during the acyclovir degradation via PMS activation [47]. It can be inferred that different Fe-based MOFs can be used as

templates to prepare different kinds of catalysts, which displayed different activation performance toward PDS/PMS. Coincidentally, catalysts with different properties and types can be obtained under different conditions of the same MOF. Li et al. controlled pyrolysis of MIL-88A(Fe) to prepare different  $\text{Fe}_x\text{C}$  composites for synergistic persulfate oxidation of phenol, in which 98.23% of phenol (20  $\text{mg L}^{-1}$ ) was degraded after 60.0 min over  $\text{Fe}_x\text{C-600/PS}$  system [48]. These catalysts can display good degradation activity toward the pollutants in the simulated sewage, however, they are prone to flocculation in the water and cause secondary pollution to the water environments. Moreover, the recovery of the catalysts from the aqueous solution is already a big problem. Thus, it is necessary to design a new type of supported catalyst, which is easy to recycle and reuse, along with free secondary pollution to the water environment.

Herein, a new supported heterogeneous catalyst  $\text{Fe}_3\text{O}_4\text{@PBS}$  ( $M\text{-Fe}_3\text{O}_4\text{-T@PBS}$ ) derived from MIL-88A/PBS was developed (Scheme 1) to accomplish photocatalysis activation of peroxydisulfate under white light for efficient TC degradation, in which the influencing factors, degradation mechanism, possible degradation pathways and toxicity evolution of TC and its intermediates were systematically studied.

## 2. Experimental

### 2.1. Materials and characterizations

All information of the chemicals and reagents, analytical methods and instruments are provided in the Supplementary Information (SI).

### 2.2. Preparation of catalysts

MIL-88A/PBS precursor: 30.0 mM fumaric acid and 30.0 mM  $\text{FeCl}_3 \cdot 6\text{H}_2\text{O}$  were dissolved in 225.0 mL ethanol and 225.0 mL deionized water, respectively. Then, four PBSs with sizes of 40.0 mm (L)  $\times$  20.0 mm (w)  $\times$  20.0 mm (h) were immersed in the  $\text{FeCl}_3$  aqueous solution for

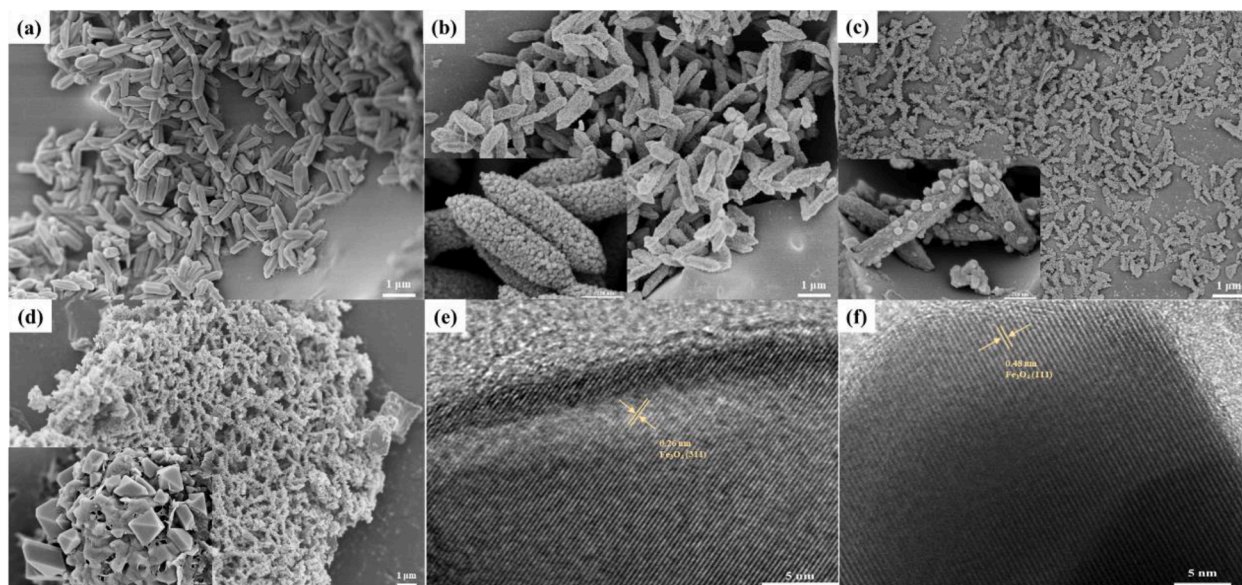


**Fig. 1.** The SEM images of (a) MIL-88A/PBS, (b) M-Fe<sub>3</sub>O<sub>4</sub>-400@PBS, (c) M-Fe<sub>3</sub>O<sub>4</sub>-500@PBS and (d) M-Fe<sub>3</sub>O<sub>4</sub>-600@PBS; the HRTEM of (e and f) M-Fe<sub>3</sub>O<sub>4</sub>-600@PBS.

20.0 min. Then, these four PBSs were transferred to the ethanol solution of fumaric acid for another 20.0 min. These in-turn immersion treatments were repeated three times. Finally, the above-mentioned two

solutions were mixed, in which the treated four PBSs were immersed under the stirring for 24 h at a speed of 150 rpm. The as-obtained MIL-88A/PBS precursors were washed with water and ethanol, respectively

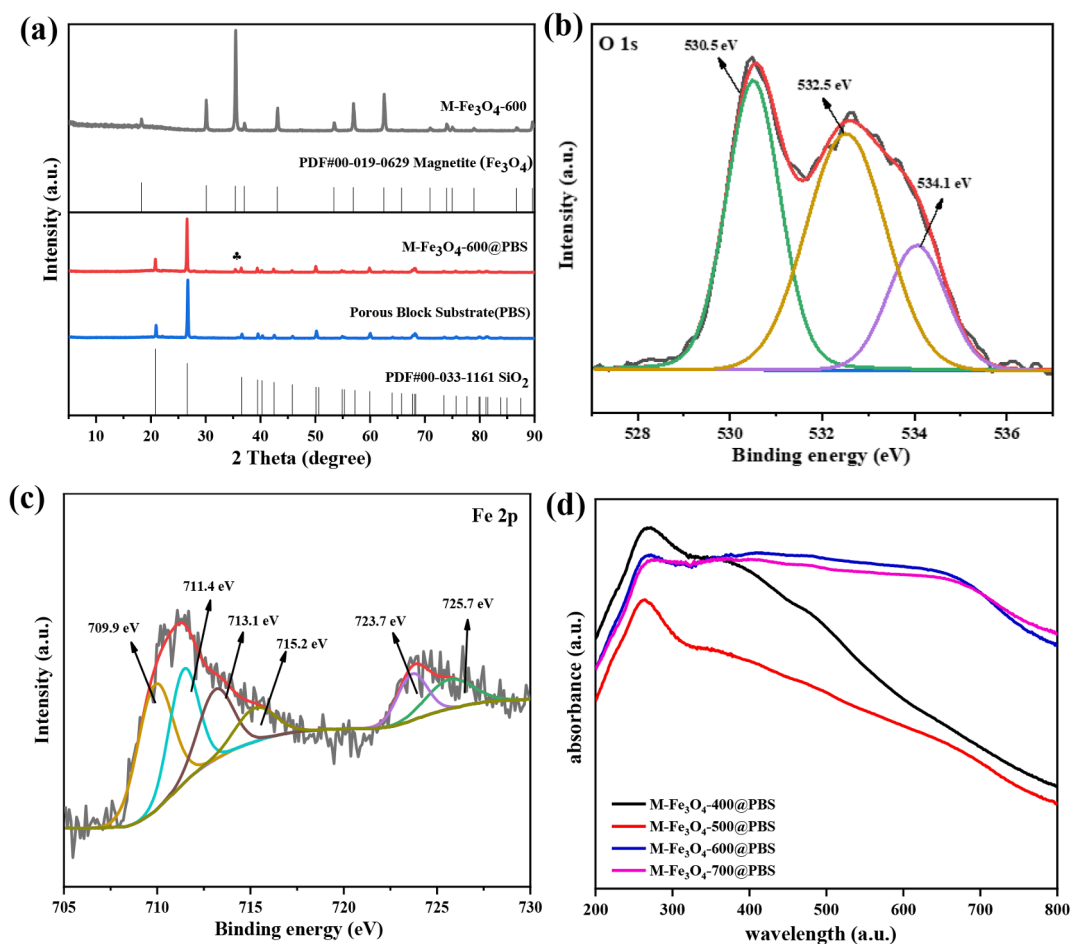


**Fig. 2.** (a) PXRD of M-Fe<sub>3</sub>O<sub>4</sub>-600 and M-Fe<sub>3</sub>O<sub>4</sub>-600@PBS. (b) O 1s high-resolution XPS spectra of the M-Fe<sub>3</sub>O<sub>4</sub>-600. (c) Fe 2p high-resolution XPS spectra of the M-Fe<sub>3</sub>O<sub>4</sub>-600@PBS catalyst. (d) The UV-Vis DRS spectra of M-Fe<sub>3</sub>O<sub>4</sub>-T@PBS.

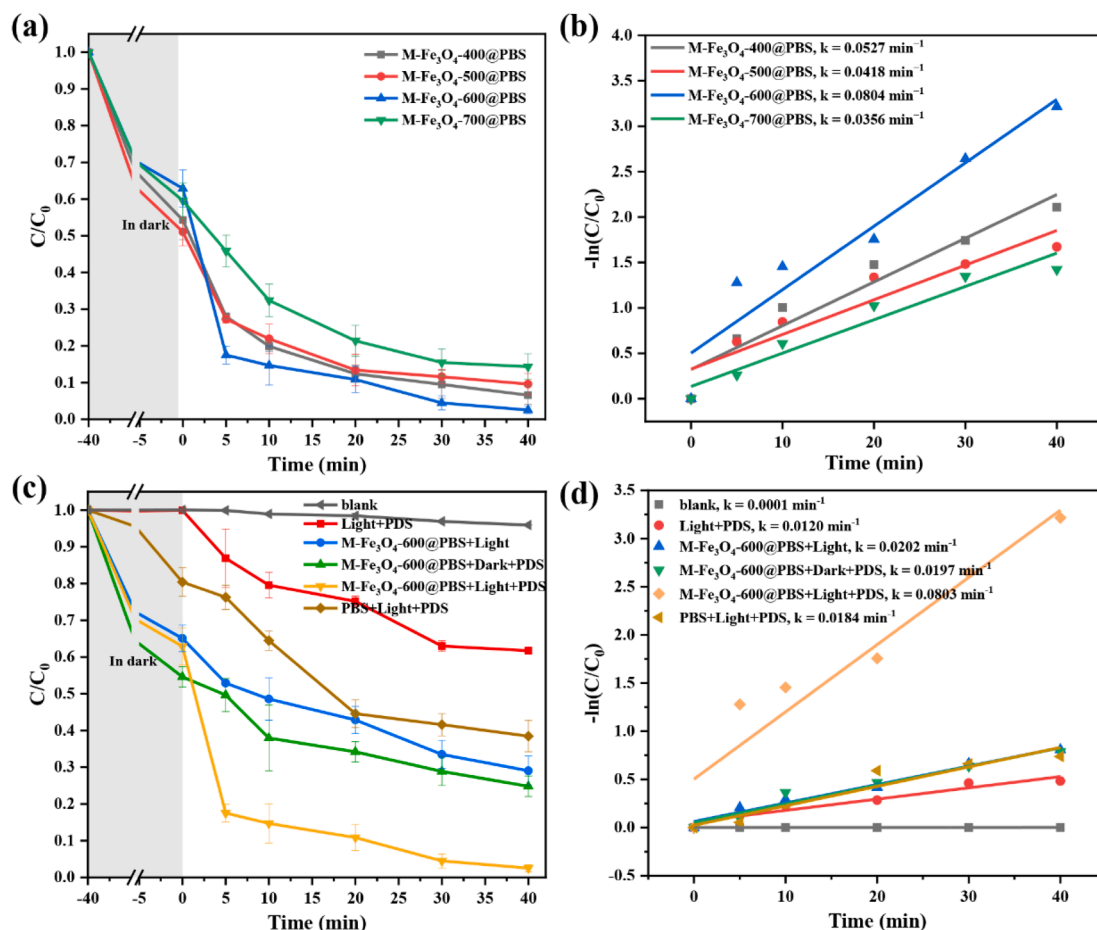


**Fig. 3.** (a) The TC degradation performances over  $M-Fe_3O_4-T@PBS$  via photocatalysis PDS activation SR-AOP under white light. (b) The  $k$  values TC degradation over different photo catalysts. (c) The TC degradation performances via photocatalysis PDS activation SR-AOP in different system. (d) The  $k$  values of TC degradation in different systems. Conditions: catalyst dosage =  $500 \text{ mg L}^{-1}$ , TC =  $10.0 \text{ mg L}^{-1}$ , pH = 4.2, PDS =  $1.5 \text{ mM}$ .

to remove unreacted fumaric acid and  $FeCl_3$ . The unloaded powder products (MIL-88A) were washed by ethanol and separated with the aid of centrifugation.

$M-Fe_3O_4-T@PBS$ : The as-prepared MIL-88A/PBS as precursor was pyrolyzed in nitrogen atmosphere with a heating rate of  $5 \text{ }^\circ\text{C min}^{-1}$  under different temperatures like  $400 \text{ }^\circ\text{C}$ ,  $500 \text{ }^\circ\text{C}$ ,  $600 \text{ }^\circ\text{C}$  and  $700 \text{ }^\circ\text{C}$  for 4 h, respectively. The black products named as " $M-Fe_3O_4-T@PBS$ " were washed with ethanol/water and dried at  $60 \text{ }^\circ\text{C}$  for 24 h, where M and T represent the magnetite and the calcination temperature, respectively. Finally, the  $M-Fe_3O_4-T$  was immobilized in porous block substrate (PBS), and the average load of each piece was  $80.0 \text{ mg}$ . As well, the pristine  $M-Fe_3O_4-T$  powder was prepared using the identical method by replacing MIL-88A/PBS with MIL-88A powder.

### 2.3. Evaluation photocatalysis activation of PDS performances over $M-Fe_3O_4-T@PBS$ composites

The TC degradation activities of  $M-Fe_3O_4-T@PBS$  via white light assisted peroxodisulfate activation were explored, in which 300 W xenon lamp without the cut-off filter was adopted as the light source (Fig. S1). The equipment setup of the photocatalysis activation of PDS for TC degradation over  $M-Fe_3O_4-T@PBS$  was shown in Fig. S2. In experiments, an as-prepared  $M-Fe_3O_4-T@PBS$  (effective catalyst dosage being  $500 \text{ mg L}^{-1}$  based on the calculated  $Fe_3O_4$ ) was added into TC aqueous solution with initial concentration of  $10 \text{ mg L}^{-1}$  (pH = 4.2). After being stirred in the dark for 40.0 min to accomplish the adsorption-desorption equilibrium,  $Na_2S_2O_8$  as PDS ( $0.15 \text{ mM}$ ) was added to the suspension upon the irradiation of white light. After pre-set interval,

$2.0 \text{ mL}$  of the filtrated solution was taken out, in which  $15 \text{ } \mu\text{L}$  of methanol was immediately added to inhibit TC from further degradation. The concentration of residual TC was measured by ultraviolet-visible spectrophotometer at the maximum absorption wavelength of  $355 \text{ nm}$  [49]. Three parallel experiments were conducted to guarantee the statistical confidence. The points in the figures were the mean value of the results, in which the error bar represents the standard deviation of the average.

## 3. Results and discussion

### 3.1. Characterization of catalysts

The successful fabrication of the MIL-88A/PBS was affirmed by the scanning electron microscope (SEM) (Fig. 1a), in which the spindle-like MIL-88A with particle size in the range of  $300 \text{ nm}$  to  $500 \text{ nm}$  were distributed in the voids of the PBS. According to the thermogravimetric analysis (TGA) results (Fig. S3), the obtained MIL-88A can be calcinated under the temperature of  $400 - 700 \text{ }^\circ\text{C}$  to potentially prepare the desired  $M-Fe_3O_4-T$ . The  $M-Fe_3O_4-400$  and  $M-Fe_3O_4-500$  in the  $M-Fe_3O_4-400@PBS$  and  $M-Fe_3O_4-500@PBS$  maintained the spindle-like rod morphology of MIL-88A (Fig. 1b and 1c). However, the particle sizes of  $M-Fe_3O_4$  in the  $M-Fe_3O_4-400@PBS$  and  $M-Fe_3O_4-500@PBS$  decreased with the increasing temperature due to the combustion of the organic ligands by pyrolysis during the thermal treatment [48,50,51]. Interestingly, the size ( $250$  to  $500 \text{ nm}$ ) of  $M-Fe_3O_4-400$  was identical to that of pristine MIL-88A, because the corresponding calcination temperature was insufficient. These observations can be affirmed by the TGA determination (Fig. S3). When the calcination temperature

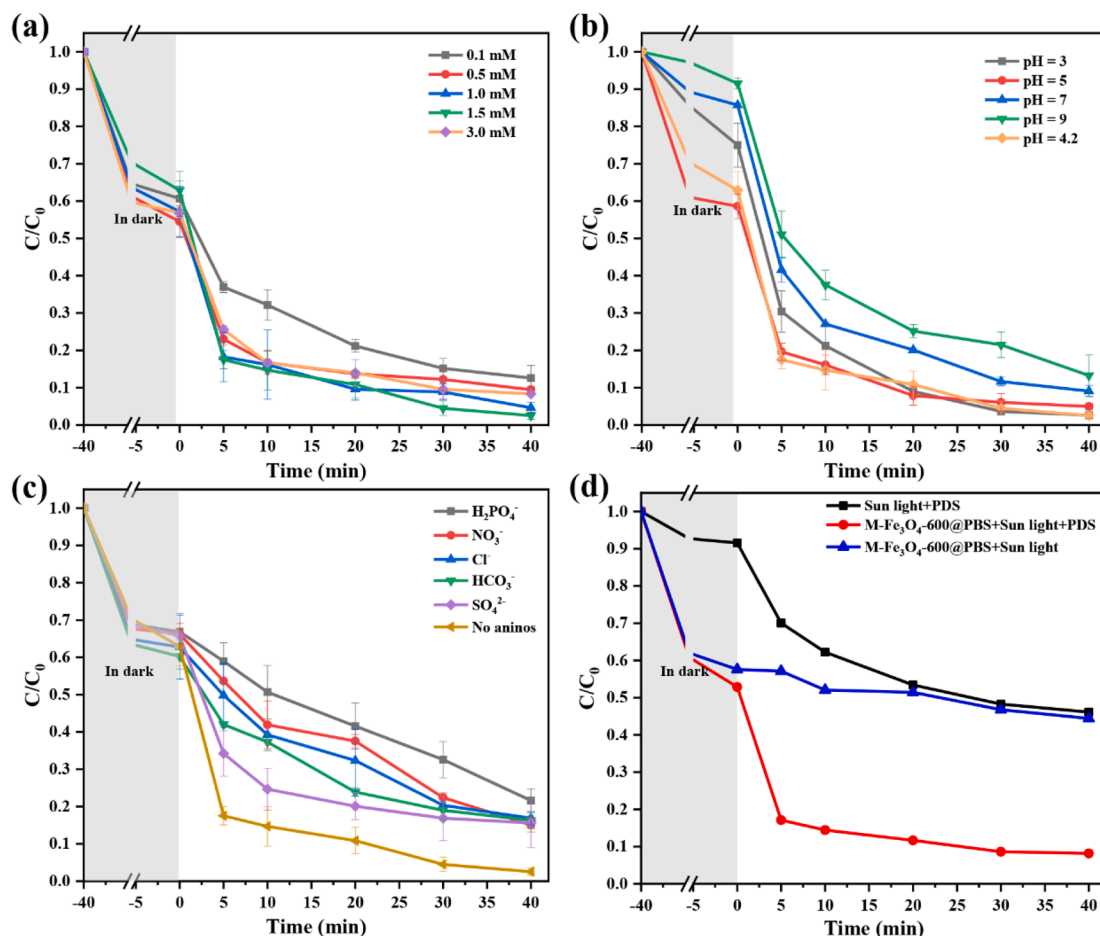


**Fig. 4.** Effects of different (a) PDS dosage, (b) pH, (c) inorganic anions on the TC degradation over M-Fe<sub>3</sub>O<sub>4</sub>-600@PBS. (d) TC degradation under real sunlight irradiation. Condition: catalyst dosage = 500 mg L<sup>-1</sup>, TC = 10.0 mg L<sup>-1</sup>, pH = 4.2, PDS = 0.15 mM. Note: Only one factor was altered, and the other factors were fixed in the Fig. 4a and b.

increased to 600 °C, M-Fe<sub>3</sub>O<sub>4</sub>-600 (as shown in Fig. 1d) in the M-Fe<sub>3</sub>O<sub>4</sub>-600@PBS displayed as cubic polyhedral nanoparticles ranging from 100 nm to 200 nm, which were embedded in the voids of PBS substrates. When the pyrolysis temperature increased to 700 °C, the spindle structure of MIL-88A(Fe) collapsed completely, which evolved into a structure with unevenly aggregated flake and layered particles (Fig. S4). Furthermore, the morphologies of individual M-Fe<sub>3</sub>O<sub>4</sub>-T illustrated in Fig. S5 were consistent with Fe<sub>3</sub>O<sub>4</sub> in the M-Fe<sub>3</sub>O<sub>4</sub>-T@PBS (T = 400–700). The HRTEM micrographs of M-Fe<sub>3</sub>O<sub>4</sub>-600@PBS (Fig. 1e and 1f) demonstrated that the fringe spacings of 0.26 nm and 0.48 nm could be assigned to the (311) and (111) crystalline facets of Fe<sub>3</sub>O<sub>4</sub> [52,53], further affirming the formation of Fe<sub>3</sub>O<sub>4</sub> in the M-Fe<sub>3</sub>O<sub>4</sub>-600@PBS. Coincidentally, the same fringe spacings were found in powder M-Fe<sub>3</sub>O<sub>4</sub>-600 (Fig. S6), demonstrating that the M-Fe<sub>3</sub>O<sub>4</sub>-600 loaded on PBS is consistent with powder M-Fe<sub>3</sub>O<sub>4</sub>-600.

Due to the minor load content of Fe<sub>3</sub>O<sub>4</sub>, it was a big challenge to characterize the composition and phase of Fe<sub>3</sub>O<sub>4</sub> in the as-prepared M-Fe<sub>3</sub>O<sub>4</sub>-600@PBS. Fortunately, the pristine M-Fe<sub>3</sub>O<sub>4</sub>-600 was produced under the identical conditions of M-Fe<sub>3</sub>O<sub>4</sub>-600@PBS. From Fig. 2a, the characteristic peaks of M-Fe<sub>3</sub>O<sub>4</sub>-600 matched well with those of the pure magnetite (Fe<sub>3</sub>O<sub>4</sub>) phase (PDF#01-088-0866), indicating that M-Fe<sub>3</sub>O<sub>4</sub>-600 could be assigned to magnetite (Fe<sub>3</sub>O<sub>4</sub>) [54]. The PXRD patterns of porous block substrate matched well with the simulated ones from PDF#00-033-1161 (SiO<sub>2</sub>) [55], indicating that the main component porous block substrate was SiO<sub>2</sub>. The characteristic peaks of M-Fe<sub>3</sub>O<sub>4</sub>-600 were masked by the primary PBS. However, the

characteristic peak of Fe<sub>3</sub>O<sub>4</sub> at 35.47° corresponding to the (311) crystal plane [54] can be observed in the PXRD patterns of the M-Fe<sub>3</sub>O<sub>4</sub>-600@PBS. In addition, the PXRD patterns of the pristine powder of M-Fe<sub>3</sub>O<sub>4</sub>-400, M-Fe<sub>3</sub>O<sub>4</sub>-500 and M-Fe<sub>3</sub>O<sub>4</sub>-700 were demonstrated in Fig. S7. The characteristic peaks of M-Fe<sub>3</sub>O<sub>4</sub>-400 and M-Fe<sub>3</sub>O<sub>4</sub>-500 matched well with those of the magnetite (Fe<sub>3</sub>O<sub>4</sub>) phase (PDF#01-088-0866). However, the metal species (Fe(III) and Fe(II)) were gradually reduced to Fe<sup>0</sup> [47,48] as the temperature increased to 700 °C, which matched well with the standard diffraction patterns of Fe<sup>0</sup> (PDF#00-006-0696).

M-Fe<sub>3</sub>O<sub>4</sub>-600 and M-Fe<sub>3</sub>O<sub>4</sub>-600@PBS were selected to explore the surface element information by X-ray photoelectron spectroscopy (XPS). The O and Fe elements were observed in the survey spectrum (Fig. S8). As shown in Fig. 2b, the O1s spectra of M-Fe<sub>3</sub>O<sub>4</sub>-600 at the positions of 530.5 eV, 532.5 eV and 534.1 eV are ascribed to lattice oxygen, adsorbed oxygen and surface oxygen [56,57]. The peaks at 709.9 eV, 711.4 eV, 713.1 eV, 723.7 eV and 725.7 eV in the Fe 2p high-resolution spectra of M-Fe<sub>3</sub>O<sub>4</sub>-600@PBS (Fig. 2c) were assigned to Fe(II) 2p<sub>1/2</sub>, Fe(III) 2p<sub>1/2</sub>, Fe(II) 2p<sub>3/2</sub>, Fe(III) 2p<sub>3/2</sub> and Fe(II) 2p<sub>3/2</sub>, respectively [58,59]. Also, the binding energy peak at 715.2 eV could be attributed to the satellite peaks of Fe 2p<sub>3/2</sub>. The existence of Fe(II) and Fe(III) further affirmed that Fe<sub>3</sub>O<sub>4</sub> was formed during the thermal treatment under 600 °C. In the Fe 2p high-resolution XPS spectra of M-Fe<sub>3</sub>O<sub>4</sub>-600 (Fig. S9), which is the same as M-Fe<sub>3</sub>O<sub>4</sub>-600@PBS, also demonstrating the successful immobilization of Fe<sub>3</sub>O<sub>4</sub>-600.

The optical absorption properties of the M-Fe<sub>3</sub>O<sub>4</sub>-T@PBS were investigated by UV-visible diffuse reflectance spectra (UV-vis DRS). As

illustrated in Fig. 2c, it can be found that the absorption edges of the as-prepared M-Fe<sub>3</sub>O<sub>4</sub>-T were similar, in which all catalysts can absorb light in both UV and visible region.

### 3.2. Photocatalysis activation of PDS degradation toward TC

#### 3.2.1. TC degradation by different catalysts

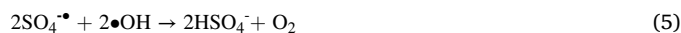
To demonstrate the potential for advanced oxidation applications, M-Fe<sub>3</sub>O<sub>4</sub>-T@PBS was used as catalyst for persulfate activation to decompose TC upon the white light illumination. The photocatalysis activation of PDS toward TC degradation efficiencies over different catalysts (including series blank conditions as control experiments) under white light and their corresponding *k* values ( $-\ln[C/C_0] = kt$ ) were demonstrated in Fig. 3a and 3b. The results revealed that the M-Fe<sub>3</sub>O<sub>4</sub>-600@PBS was the optimal catalyst (0.0804 min<sup>-1</sup>), which were 1.52, 1.92 and 2.25 times higher than those of M-Fe<sub>3</sub>O<sub>4</sub>-400@PBS (0.0507 min<sup>-1</sup>), M-Fe<sub>3</sub>O<sub>4</sub>-500@PBS (0.0418 min<sup>-1</sup>) and M-Fe<sub>3</sub>O<sub>4</sub>-700@PBS (0.0356 min<sup>-1</sup>). It was reported that the PDS/PMS activation performances of the catalysts would be affected by the structure and physical-chemical properties of the catalysts [48,60,61]. It had been demonstrated that M-Fe<sub>3</sub>O<sub>4</sub>-400 and M-Fe<sub>3</sub>O<sub>4</sub>-500 possessed similar morphology which maintained the spindle-like rod morphology of MIL-88A. However, the M-Fe<sub>3</sub>O<sub>4</sub>-600 in the M-Fe<sub>3</sub>O<sub>4</sub>-600@PBS displayed as cubic polyhedral nanoparticles. Therefore, M-Fe<sub>3</sub>O<sub>4</sub>-400@PBS and M-Fe<sub>3</sub>O<sub>4</sub>-500@PBS were considered as partially derivative. Nevertheless, M-Fe<sub>3</sub>O<sub>4</sub>-600@PBS was complete derivatization, which was inclined to expose more active sites to activate PDS for TC degradation. In addition, more and more iron oxides were gradually reduced to Fe<sup>0</sup> as the pyrolysis temperature further increased to 700 °C. Due to the instantaneous reaction property and leaching of Fe<sup>0</sup> [62] as well as the collapse of structure, the TC degradation efficiency of M-Fe<sub>3</sub>O<sub>4</sub>-700@PBS is slower than that of M-Fe<sub>3</sub>O<sub>4</sub>-600@PBS. Hence, the M-Fe<sub>3</sub>O<sub>4</sub>-600@PBS was deemed as the optimal catalyst for the subsequent experiments.

As displayed in Fig. S10, the TC adsorption equilibrium over M-Fe<sub>3</sub>O<sub>4</sub>-600@PBS was accomplished within 40.0 min, in which ca. 39.7% TC can be adsorptively removed. As depicted in Fig. 3c, the direct TC degradation was not significant (4.1%) in the absence of both catalyst and PDS under white light illumination, demonstrating that the TC displayed high photo-stability. The TC degradation efficiencies increased from 4.1% in the light system to 38.2% in the light/PDS system within 40.0 min, indicating that some active species could be yielded to degrade TC via individual photo-induced PDS activation [16]. As shown in Table S2, the TC removal efficiency also reached 61.5% in the PBS/light/PDS system due to that the commercial substrate used for loading contains some metal impurities. This catalytic efficiency over pristine PBS was not enough for practical application in engineering. The addition of PDS can boost the catalytic efficiency of the M-Fe<sub>3</sub>O<sub>4</sub>-600@PBS/light/PDS system, in which 97.5% of TC can be oxidatively upon the white light illumination for 40.0 min, higher than those of M-Fe<sub>3</sub>O<sub>4</sub>-600@PBS/light (70.9%) and M-Fe<sub>3</sub>O<sub>4</sub>-600@PBS/Dark/PDS (75.2%), respectively. The corresponding *k* values (Fig. 3d) of different reaction systems displayed that the M-Fe<sub>3</sub>O<sub>4</sub>-600@PBS/light/PDS system exhibited superior photocatalytic activity toward TC degradation. Therefore, the following experiments were carried out in M-Fe<sub>3</sub>O<sub>4</sub>-600@PBS/light/PDS system due to the excellent catalytic performance of M-Fe<sub>3</sub>O<sub>4</sub>-600@PBS/Light/PDS.

#### 3.2.2. Effect of PDS dosage on TC degradation

The effect of PDS dosage (0.1, 0.5, 1, 1.5 and 3.0 mM) on TC removal was investigated (Fig. 4a). When the PDS concentration increased from 0.1 to 1.5 mM, the TC removal efficiencies increased from 87.4% to 97.5% within 40.0 min upon the irradiation of white light. This can be ascribed to the higher PDS concentration could produce more reactive oxygen species (ROS) to enhance the TC degradation. But the corresponding degradation efficiency of TC decreased as the PDS dosage

increased to 3 mM. The above experimental phenomenon can be ascribed to the quench of both sulfate and hydroxyl radicals with excessive PDS according to the reactions Eqs. (1) and (2) [63]. In addition, when PDS concentration was excessive, the reactions expressed in Eqs. (3)–(5) resulted into the reducing availability of these radicals for TC degradation [64]. As well, with the fixed amount of catalyst, the output of photo-generated electrons and holes were constant, which failed to meet the requirement of the excessive PDS as electron acceptors in the reaction illustrated in Eq. (6) [65], thus the degradation efficiency attained a stable plateau. Hence, the optimal dosage of PDS was selected as 1.5 mM.



#### 3.2.3. Effect of initial pH on TC degradation

The surface charge properties of the catalyst, the interaction between the surface of the catalyst and the targeted organic molecules along with the reaction between active radicals can be heavily affected by pH [66]. The effect of initial pH values on the photocatalysis activation of PDS TC degradation over M-Fe<sub>3</sub>O<sub>4</sub>-600@PBS was explored (Fig. 4b). The pH was controlled using 0.1 mM H<sub>2</sub>SO<sub>4</sub> and NaOH. The results demonstrated that the TC decomposition in the M-Fe<sub>3</sub>O<sub>4</sub>-600@PBS/light/PDS system was effective over a wide pH range upon 40.0 min of white light irradiation. But it can be observed that with the increase of pH value of the solution, the removal rate of TC decreased. There were two main reasons for this phenomenon. Firstly, more SO<sub>4</sub><sup>•-</sup> radicals can be produced under an acidic environment according to Eqs. (7) and (8). Secondly, the increasing H<sup>+</sup> can lead to more hydroxyl radical formation according to Eqs. (9)–(11). Another noteworthy phenomenon was that the adsorption capacity of the catalyst in different solutions was also different over the dark condition. When the corresponding pH was 3.0, 4.2, 5.0, 7.0 and 9.0, the dark adsorption capacity of the catalyst is 25.0%, 41.4%, 37.1%, 14.3% and 8.5% respectively. These phenomena should be ascribed to the surface electrical properties of M-Fe<sub>3</sub>O<sub>4</sub>-600@PBS and the morphology of TC molecule at different pH values. TC is an amphoteric molecule with pK<sub>a</sub> values of 3.3, 7.7 and 9.7 [67]. The TC can lose the proton to form negative TCH<sup>-</sup> and TC<sup>2-</sup> at pH > 6.0, which displayed electrostatic repulsion with M-Fe<sub>3</sub>O<sub>4</sub>-600@PBS due to their negative zeta potentials (Fig. S11). As pH < 6.0, the TC molecules are in the forms of both neutral TC and positively charged TCH<sup>3+</sup> specie, which facilitated the TC molecule adsorption of M-Fe<sub>3</sub>O<sub>4</sub>-600@PBS at pH = 4.2 and 5.0. In contrast, the zeta potential was positive at pH = 3.0, which restrained the adsorption toward TC molecule. Because of electrostatic interaction, more TC could be adsorbed at pH = 4.2 and pH = 5.0 than those at pH = 3.0, 7.0 and 9.0.



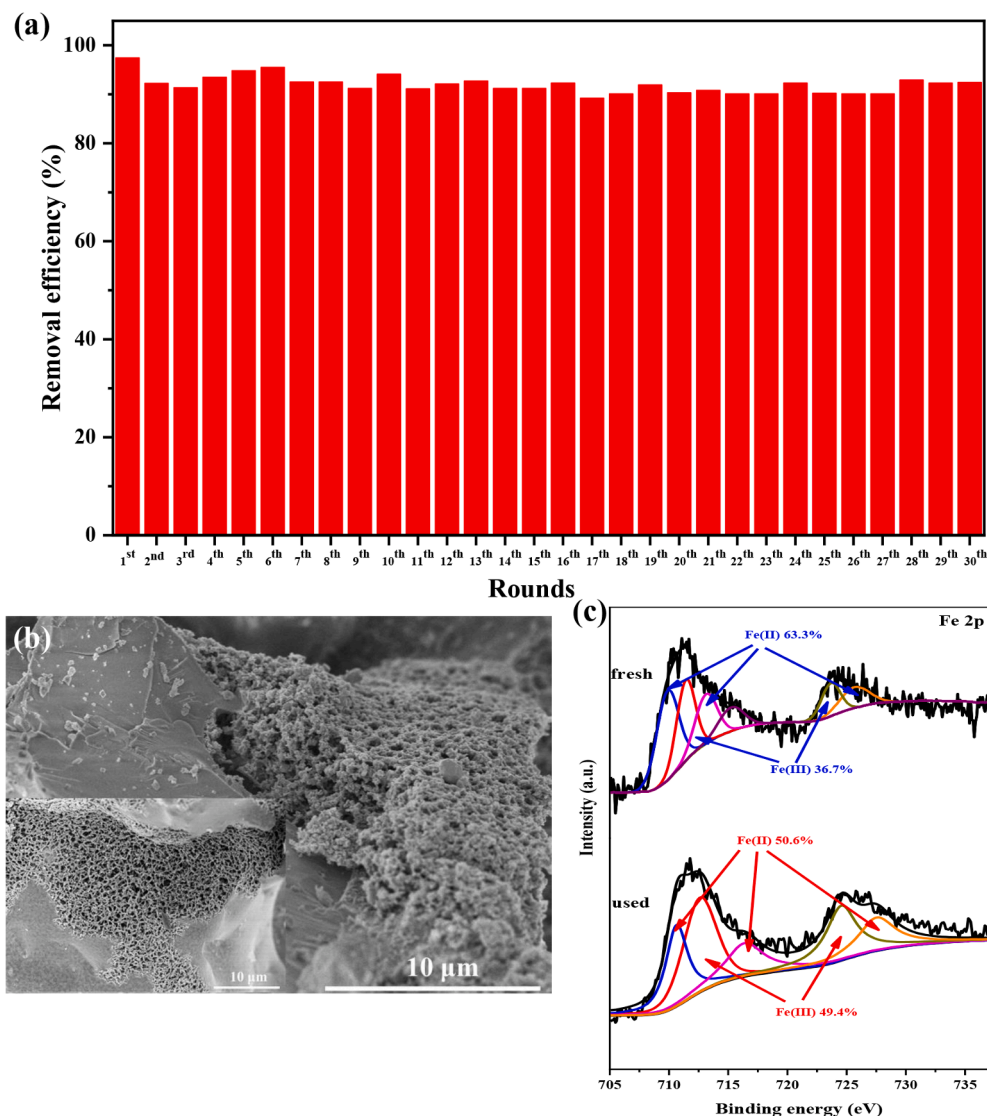


**Fig. 5.** (a) Reusability tests with M-Fe<sub>3</sub>O<sub>4</sub>-600@PBS for TC degradation. Condition: catalyst dosage = 500 mg L<sup>-1</sup>, TC = 10.0 mg L<sup>-1</sup>, pH = 4.2, PDS = 0.15 mM. (b) SEM images before (inset) and after 30 cycles. (c) Fe 2p high-resolution XPS spectra of M-Fe<sub>3</sub>O<sub>4</sub>-600@PBS after 30 cycles.

### 3.2.4. Effect of inorganic anions on TC degradation

It has been reported that the degradation of tetracycline antibiotics in aqueous solutions may be inhibited by the co-existing inorganic anions [68]. To investigate the practical applications of M-Fe<sub>3</sub>O<sub>4</sub>-600@PBS/light/PDS system, the simulated wastewater samples were prepared by dissolving the tetracycline antibiotics matrix into an aqueous solution containing different inorganic ions like H<sub>2</sub>PO<sub>4</sub><sup>-</sup>, Cl<sup>-</sup>, HCO<sub>3</sub><sup>-</sup> and NO<sub>3</sub><sup>-</sup>. All concentrations of the ions mentioned above were referred from the surface water quality in Beijing [69–71].

The effect of inorganic anions on TC degradation followed the order of no anions (97.5%) > NO<sub>3</sub><sup>-</sup> (94.7%) > H<sub>2</sub>PO<sub>4</sub><sup>-</sup> (91.4%) > HCO<sub>3</sub><sup>-</sup> (84.7%) > Cl<sup>-</sup> (82.0%), suggesting that the Cl<sup>-</sup> exerted the highest impact among the all selected inorganic ions with the introduction of Cl<sup>-</sup>, NO<sub>3</sub><sup>-</sup>, HCO<sub>3</sub><sup>-</sup> and H<sub>2</sub>PO<sub>4</sub><sup>-</sup> being 135.30, 13.60, 272.00 and 0.85 mg L<sup>-1</sup>, respectively (Fig. 4c). The experimental results showed that the TC removal efficiencies over M-Fe<sub>3</sub>O<sub>4</sub>-600@PBS decreased with the presence of various inorganic anions. The above results can be attributed to inorganic anions like H<sub>2</sub>PO<sub>4</sub><sup>-</sup>, Cl<sup>-</sup>, HCO<sub>3</sub><sup>-</sup> and NO<sub>3</sub><sup>-</sup>, may act as reactants to convert the more active radicals to less active ones or as scavengers to consume these radicals [68,72,73]. The downside impact of the inorganic ions can be overcome by some approaches like increasing the catalyst dosage or/and prolonging hydraulic retention

time (HRT) in the real situation [40].

### 3.2.5. TC degradation under real sunlight irradiation

Considering that M-Fe<sub>3</sub>O<sub>4</sub>-600@PBS could accomplish outstanding photocatalysis performances under white light, it might achieve the identically preferable photocatalysis activation of persulfate under real sunlight. In this study, from this point, series experiments were performed under real sunlight (the spectrum and experimental devices being displayed in Fig. S12 and Fig. S13) at the Daxing campus of BUCEA (39°44' N, 116°17' E) on November 29th, 2020 (3 °C). The average optical power was 22.33 mW cm<sup>-2</sup>. As shown in Fig. 4d, the TC degradation efficiency in the real sunlight/PDS system and M-Fe<sub>3</sub>O<sub>4</sub>-600@PBS/real sunlight system were 58.9% and 55.8%, respectively. It was worth noting that the TC degradation efficiency could reach 91.8% under the identical condition in the M-Fe<sub>3</sub>O<sub>4</sub>-600@PBS/real sunlight/PDS system after 40.0 min's illumination, which was comparable with the degradation performance under white light. This proved that the as-prepared M-Fe<sub>3</sub>O<sub>4</sub>-600@PBS catalyst demonstrated good application prospects in real sunlight, which could achieve the goal of energy-saving.

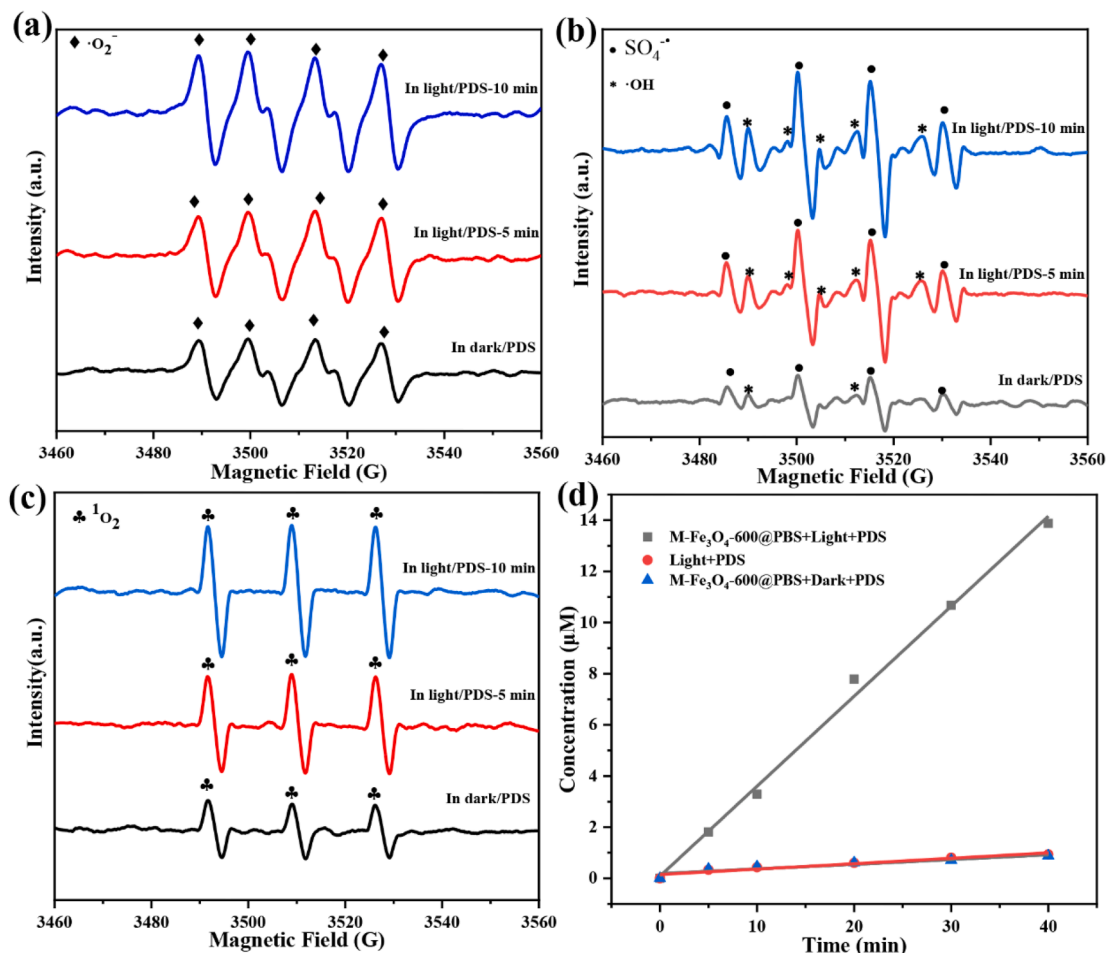


Fig. 6. The ESR spectra of (a)  $\text{DMPO}\cdot\text{O}_2^-$ , (b)  $\text{DMPO}\cdot\text{SO}_4^{\cdot-}$  and  $\text{DMPO}\cdot\text{OH}$  and (c)  $\text{TEMP}\cdot^1\text{O}_2$  over  $\text{M}\text{-Fe}_3\text{O}_4\text{-600@PBS}$ /light/PDS system. (d) The  $\text{SO}_4^{\cdot-}$  radicals concentrations yielded in different systems.

### 3.2.6. Reusability and stability of $\text{M}\text{-Fe}_3\text{O}_4\text{-600@PBS}$ composites

The stability and long-term recyclability of the catalysts are important factors to reduce the cost of pollutant control [74,75]. Before using, the as-synthesized materials were washed with water and ethanol 5 times to clean the labile catalysts on the PBS and reduced the dissolution of Fe ions. After each cycles experiment, the  $\text{M}\text{-Fe}_3\text{O}_4\text{-600@PBS}$  was only washed with deionized water and dried at  $60^\circ\text{C}$  for 4 h. From Fig. 5a, it could be observed that the TC removal efficiency over  $\text{M}\text{-Fe}_3\text{O}_4\text{-600@PBS}$  was maintained after 30 cycles' operation, demonstrating the superior stability and long-lasting reusability of the catalysts. The fluctuations in the TC degradation efficiencies in every cycle was within 5%, which could be related to the artificially controlled experimental conditions including but not limited to the mode of operation and flow rate. The adsorption efficiencies over  $\text{M}\text{-Fe}_3\text{O}_4\text{-600@PBS}$  of all cycles were demonstrated in Fig. S14. It was found that the adsorption efficiency of  $\text{M}\text{-Fe}_3\text{O}_4\text{-600@PBS}$  at the 30th cycle toward TC could still reach to 36.5%. It was deemed that TC adsorbed on the  $\text{M}\text{-Fe}_3\text{O}_4\text{-600@PBS}$  was degraded during the photocatalysis PDS activation SR-AOP, which was affirmed by the continuous excellent adsorption performance. It can also be seen that the weight of the immobilized catalyst was unchanged after 30 cycles. The ICP-OES data (Fig. S15) displayed that the concentrations of the leached Fe ions after each cycle was maintained at ca.  $0.27\text{-}0.59\text{ mg L}^{-1}$ , which conformed to the integrated discharge standard of water pollutants ( $2\text{ mg L}^{-1}$ ) set by the corresponding Beijing standard (DB11/307-2013).

To further highlight the advantage of the immobilized magnetite ( $\text{Fe}_3\text{O}_4$ ) onto porous block substrate (PBS), the photocatalysis activation of PDS performance of powder  $\text{Fe}_3\text{O}_4$  was compared with

$\text{M}\text{-Fe}_3\text{O}_4\text{-600@PBS}$  under identical conditions. The results show that after reaction, the aqueous solution treated using  $\text{Fe}_3\text{O}_4$  powder was turbid due to the suspended  $\text{Fe}_3\text{O}_4$ , while the solution treated by  $\text{M}\text{-Fe}_3\text{O}_4\text{-600@PBS}$  was clear and free of suspended black particles (Fig. S16).

It was observed that the morphology and structure of  $\text{M}\text{-Fe}_3\text{O}_4\text{-600@PBS}$  were still maintained after 30 cycles, which was affirmed by the SEM observation of  $\text{M}\text{-Fe}_3\text{O}_4\text{-600@PBS}$  (Fig. 5b), indicating the good stability and reusability of  $\text{M}\text{-Fe}_3\text{O}_4\text{-600@PBS}$ . The high-resolution Fe 2p spectrum of the fresh and used  $\text{M}\text{-Fe}_3\text{O}_4\text{-600@PBS}$  was illustrated in Fig. 5c, in which the peaks at 712.1 and 724.6 eV were deemed to correspond to Fe 2p<sub>1/2</sub> and Fe 2p<sub>3/2</sub>, respectively. As well, the peaks of Fe(II) and Fe(III) were observed in the Fe 2p spectra of both the fresh and used  $\text{M}\text{-Fe}_3\text{O}_4\text{-600@PBS}$ . Clearly, the proportion of Fe(II) species in  $\text{M}\text{-Fe}_3\text{O}_4\text{-600@PBS}$  declined from 63.3% for the fresh sample to 50.6% for the used one, indicating that the oxidation of Fe(II) into Fe(III) species occurred on the surface of  $\text{M}\text{-Fe}_3\text{O}_4\text{-600@PBS}$ . From the SEM-EDS elemental mapping (Fig. S17), there were no significant changes in the content of C, Fe and O. It was worth mentioning that the content of N increased obviously, which was caused by the adsorption of TC. All evidence demonstrated the excellent recyclability of the catalyst prepared.

### 3.3. Proposed degradation mechanism

It can be seen from Fig. S18 that the electrochemical impedance spectra (EIS) arc radius of  $\text{M}\text{-Fe}_3\text{O}_4\text{-600@PBS}$ /light/PDS was smaller than those of  $\text{M}\text{-Fe}_3\text{O}_4\text{-600@PBS}$ /dark,  $\text{M}\text{-Fe}_3\text{O}_4\text{-600@PBS}$ /light

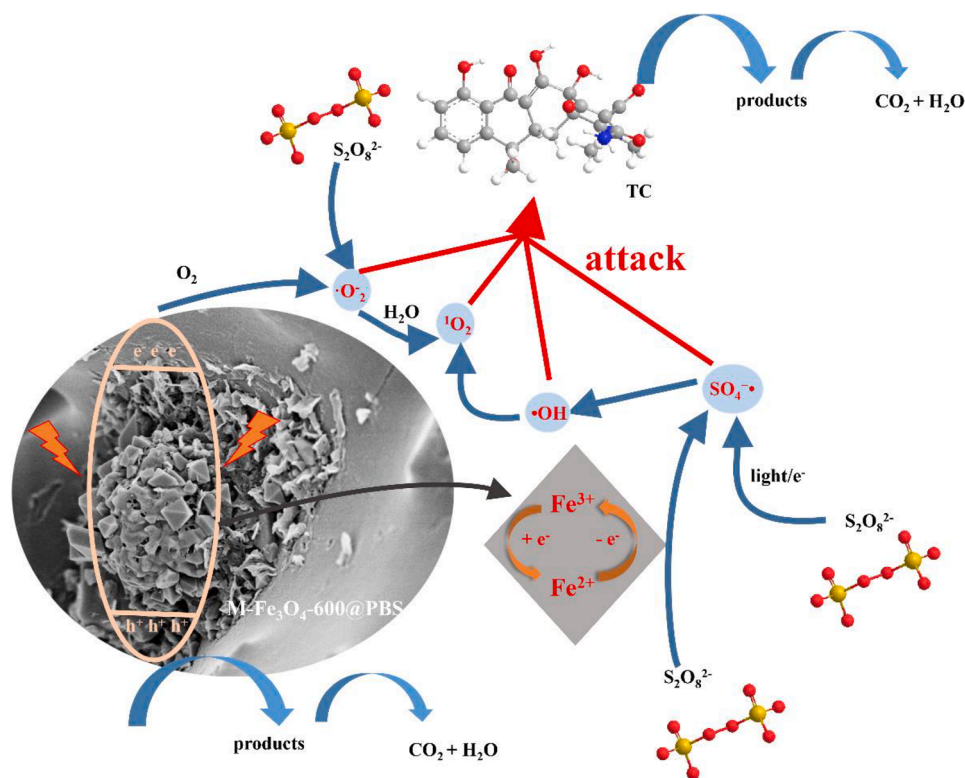


Fig. 7. The possible mechanisms for TC decomposition over M-Fe<sub>3</sub>O<sub>4</sub>-600@PBS/light/PDS system.

and M-Fe<sub>3</sub>O<sub>4</sub>-600@PBS/dark/PDS, indicating M-Fe<sub>3</sub>O<sub>4</sub>-600@PBS/light/PDS system was more beneficial to inhibit the recombination of photogenerated electrons and hole [76]. In our study, the pristine M-Fe<sub>3</sub>O<sub>4</sub>-600 was adopted to carry out the Motte-Schottky measurements, considering that the PBS acted as substrate. As depicted in Fig. S19, the positive relationship between the slope of  $C^2$  value and the potential in Motte-Schottky measurements affirmed the M-Fe<sub>3</sub>O<sub>4</sub>-600 as the n-type semiconductor [77,78]. The conduction band (CB) of M-Fe<sub>3</sub>O<sub>4</sub>-600 was determined as ca. -0.56 eV versus the Ag/AgCl electrode via the Motte-Schottky tests. For n-type semiconductors, the position of EFB is generally ca. 0.1 eV higher than that of ECB. Also, the valence band (VB) of M-Fe<sub>3</sub>O<sub>4</sub>-600 was modified by the formula  $E = E_0 - 0.05915 \times \text{pH}$ , taking account of the effect of pH value (pH = 7) [79]. Therefore, the VB of M-Fe<sub>3</sub>O<sub>4</sub>-600 was -0.87 eV vs. NHE at pH = 7.0. The bandgap ( $E_g$ ) (Fig. S20) of M-Fe<sub>3</sub>O<sub>4</sub>-600 was estimated as 1.48 eV using  $(Ah\nu)^2$  versus  $h\nu$  [80]. The VB potential of M-Fe<sub>3</sub>O<sub>4</sub>-600 was calculated as 0.61 eV vs. Ag/AgCl ( $E_{CB} = E_{VB} - E_g$ ) based on the band gap of 1.48 eV. As the redox potential value of CB (-0.87 eV vs. NHE) is higher than that of O<sub>2</sub>/•O<sub>2</sub><sup>-</sup> (-0.33 eV vs. NHE), it was reasonable that •O<sub>2</sub><sup>-</sup> radicals were produced [81].

The main active species formed during the reaction process was identified by active substance trapping experiments. A series of active species quenching agents including methyl alcohol (MeOH), t-butanol (TBA), N<sub>2</sub>, L-Histidine and triethanolamine (TEA) were selected to capture SO<sub>4</sub><sup>•-</sup>, •OH, •O<sub>2</sub><sup>-</sup>, <sup>1</sup>O<sub>2</sub> and h<sup>+</sup>, respectively. As shown in Fig. S21, the corresponding degradation efficacy reduced by 37.8% with the introduction of MeOH, implying that the SO<sub>4</sub><sup>•-</sup> radicals primarily attacked the TC molecules. The inhibition effects after the introduction of N<sub>2</sub> (22.6%), TBA (13.6%) and L-Histidine (24.4%), implying that •O<sub>2</sub><sup>-</sup>, •OH and <sup>1</sup>O<sub>2</sub> were the important active species to decompose TC. When TEA was introduced into M-Fe<sub>3</sub>O<sub>4</sub>-600@PBS/light/PDS system, the catalytic removal rate of TC decreased by 14.7%, implying that holes also participated in the degradation toward TC.

To clarify the active substances yield in the SR-AOPs reaction, the radicals (•O<sub>2</sub><sup>-</sup>, SO<sub>4</sub><sup>•-</sup> and •OH) and <sup>1</sup>O<sub>2</sub> produced by

M-Fe<sub>3</sub>O<sub>4</sub>-600@PBS in dark and white light irradiation were qualitatively determined by electron spin resonance (ESR). It can be seen in Fig. 6a, the peaks of •O<sub>2</sub><sup>-</sup> could be found in the M-Fe<sub>3</sub>O<sub>4</sub>-600@PBS/PDS system, which attributed to the hydrolysis of S<sub>2</sub>O<sub>8</sub><sup>2-</sup> (Eqs. (12) and (13)). However, the signals of •O<sub>2</sub><sup>-</sup> were much stronger in the M-Fe<sub>3</sub>O<sub>4</sub>-600@PBS/light/PDS system because •O<sub>2</sub><sup>-</sup> was also produced via the reduction of O<sub>2</sub> (Eq. (14)) over white light irradiation. It can be seen in Fig. 6b clearly, weak peaks of SO<sub>4</sub><sup>•-</sup> and •OH could be found in the Fe<sub>3</sub>O<sub>4</sub>-600@PBS/PDS system. Nevertheless, under white light irradiation for 5.0 min and 10.0 min, the intensities of the SO<sub>4</sub><sup>•-</sup> and •OH increased significantly because of the interactions between SO<sub>4</sub><sup>•-</sup> and H<sub>2</sub>O/OH<sup>-</sup> (Eqs. (15) and (16)). The remarkable increase of SO<sub>4</sub><sup>•-</sup> signals was contributed to that PDS could be activated not only by the cycle of Fe(III)/Fe(II) in M-Fe<sub>3</sub>O<sub>4</sub>-600@PBS via Eqs. (17) and (18), but also by the photo-generated electrons via Eqs. (19) and (20). As shown in Fig. 6c, the TEMP-<sup>1</sup>O<sub>2</sub> signals were both detected in M-Fe<sub>3</sub>O<sub>4</sub>-600@PBS/PDS and M-Fe<sub>3</sub>O<sub>4</sub>-600@PBS/light/PDS systems. The weak signal <sup>1</sup>O<sub>2</sub> in M-Fe<sub>3</sub>O<sub>4</sub>-600@PBS/PDS system could be attributed to the formation of •O<sub>2</sub> and <sup>1</sup>O<sub>2</sub> from the slow PDS hydrolysis (Eqs. (12), (13) and (21)). Among them, the <sup>1</sup>O<sub>2</sub> characteristic peak in the M-Fe<sub>3</sub>O<sub>4</sub>-600@PBS/light/PDS system was much stronger than that in M-Fe<sub>3</sub>O<sub>4</sub>-600@PBS/PDS system. It was mainly due to the production of more •O<sub>2</sub> and •OH in the light condition and thus the production of more singlet oxygen (Eqs. (14), (16) and (22)). In all, it was deemed that •O<sub>2</sub>, •OH, SO<sub>4</sub><sup>•-</sup>, and <sup>1</sup>O<sub>2</sub> contributed simultaneously to the TC degradation.

To further evidence the generation of SO<sub>4</sub><sup>•-</sup> radicals in the M-Fe<sub>3</sub>O<sub>4</sub>-600@PBS/light/PDS system, the SO<sub>4</sub><sup>•-</sup> concentration was quantified by detecting the reaction by-product BQ generated from the SO<sub>4</sub><sup>•-</sup> oxidation of HBA (Eq. (23)) [82]. As shown in Fig. 6d, SO<sub>4</sub><sup>•-</sup> production increased with reaction time to 13.88 μM at 40.0 min in M-Fe<sub>3</sub>O<sub>4</sub>-600@PBS/light/PDS system. To be specific, the concentration of SO<sub>4</sub><sup>•-</sup> was only 0.93 and 0.88 μM in light/PDS and M-Fe<sub>3</sub>O<sub>4</sub>-600@PBS/PDS system by the same experimental method. This phenomenon was consistent with the results of ESR. It was also

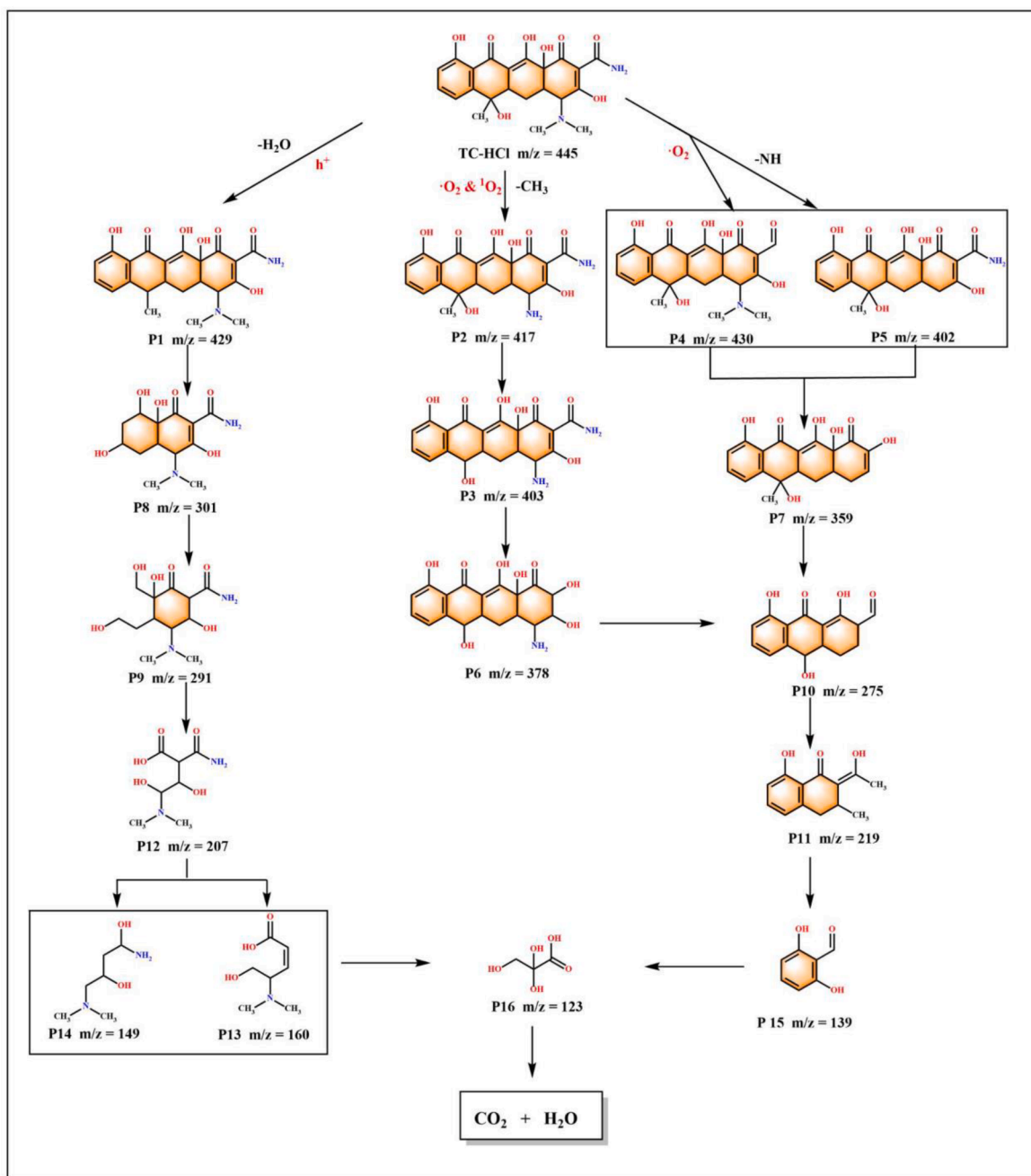
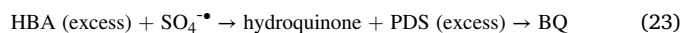
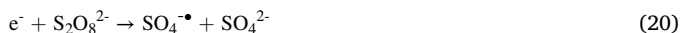
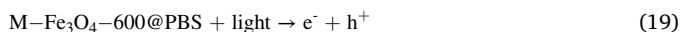
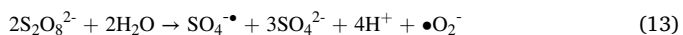


Fig. 8. Proposed TC degradation pathways in the M-Fe<sub>3</sub>O<sub>4</sub>-600@PBS/light/PDS system.

proved that  $SO_4^{\bullet-}$  played an important role in the degradation of TC.



The photocatalysis activation PDS and the corresponding TC degradation mechanism over M-Fe<sub>3</sub>O<sub>4</sub>-600@PBS as catalyst was shown in Fig. 7. (1) PDS can be activated by the direct electron transfer to yield  $SO_4^{\bullet-}$  radicals in solution, as well, some free photo-excited electrons can react with dissolved oxygen (DO) molecules to yield both  $\bullet OH$  and  $\bullet O_2^-$  radicals. (2) The  $S_2O_8^{2-}$  is activated by white light to yield  $SO_4^{\bullet-}$  radicals in solution, where the formed  $SO_4^{\bullet-}$  radicals might be partially transformed into  $\bullet OH$  and  $\bullet O_2^-$ . (3) The photogenerated electrons facilitate the in-situ redox cycles of Fe(II)/Fe(III) in M-Fe<sub>3</sub>O<sub>4</sub>-600@PBS, which

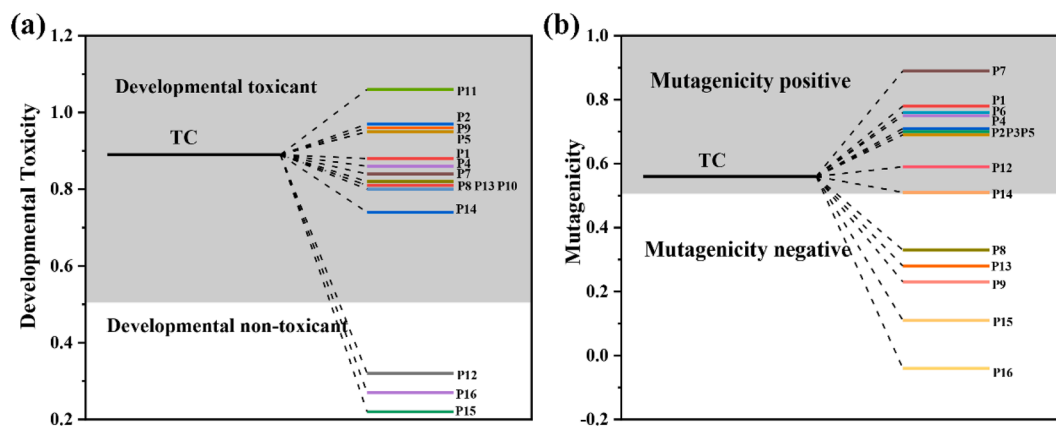


Fig. 9. (a) Developmental toxicity and (b) mutagenicity of TC and degradation intermediates.

promoted the PDS activation to yield  $\text{SO}_4^{\bullet-}$  radicals to improve the TC degradation performance. (4) The photogenerated holes can be directly involved in the TC decomposition to synchronously boost the electron-hole separation.

### 3.4. Intermediates and possible degradation pathways of TC

As shown in Fig. S22, 37.8% of TOC was removed over M- $\text{Fe}_3\text{O}_4$ -600/light/PDS system, indicating that TC can be partly mineralized into  $\text{CO}_2$  and  $\text{H}_2\text{O}$ . In this study,  $\text{SO}_4^{\bullet-}$ ,  $\bullet\text{OH}$ ,  $\bullet\text{O}_2^-$ ,  $^1\text{O}_2$  and  $\text{h}^+$  were determined as the primary reactive species in the M- $\text{Fe}_3\text{O}_4$ -600@PBS/light/PDS system. Both of those radicals were electrophilic species [40]. It was previously reported that the Fukui index of TC based on its population analysis (NPA) charge distribution of TC molecule was calculated to clarify the nucleophilic ( $f^+$ ) and electrophilic attack ( $f^-$ ) in the presence of different free radicals [83]. The HOMO orbitals which potentially lose electrons during an electrophilic attack of tetracycline was localized on the C1–C6 ring [83]. As shown in Fig. 8, based upon the UPLC-MS products identification (Fig. S23) and previous results, three possible pathways of TC were proposed. (1) The TC molecules were transformed into P1 ( $m/z = 427$ ) via the dehydration process under the action of  $\text{h}^+$  [81]. (2) TC was decomposed to P2 ( $m/z = 417$ ) and P3 ( $m/z = 403$ ) successively by losing methyls under the oxidation of  $\text{O}_2^-$  and  $^1\text{O}_2$  [83,84]. (3) The P4 ( $m/z = 430$ ) and P5 ( $m/z = 402$ ) were produced through the deamination reaction mainly under the attack of  $\text{O}_2^-$  [81]. With the progress of the reaction, several intermediates ( $m/z = 378, 359, 301, 291, 275, 219, 207, 160, 149$  and  $123$ ) were produced by terminal oxidation and ring-opening reaction triggered by  $\bullet\text{OH}$ ,  $\text{SO}_4^{\bullet-}$ ,  $\text{O}_2^-$  and  $^1\text{O}_2$  [85,86]. Finally, small molecular intermediate products would be completely mineralized to  $\text{CO}_2$  and  $\text{H}_2\text{O}$  over the catalysts.

The toxicities of by-products were necessary to be considered in the TC degradation. The developmental toxicity and mutagenicity of TC and its by-products were assessed by using Toxicity Estimation Software Tool (T.E.S.T.) based on quantitative structure–activity relationship (QSAR) model [87]. TC was defined as a “developmental toxicant”, while the oxidative degradation reaction could lower the toxicity, in which the intermediates of P12, P15 and P16 were even defined as “developmental non-toxicant” (Fig. 9a). The degradation reaction in M- $\text{Fe}_3\text{O}_4$ -600@PBS/light/PDS system can reduce the mutagenicity of TC (Fig. 9b). The comprehensive analyses results showed that photocatalysis activation of PDS process over M- $\text{Fe}_3\text{O}_4$ -600@PBS system could form less toxic intermediates and even achieve complete mineralization.

## 4. Conclusion

Supported MIL-88A derivative catalyst (M- $\text{Fe}_3\text{O}_4$ -T@PBS) was

prepared for the first time. As a heterogeneous catalyst, the M- $\text{Fe}_3\text{O}_4$ -600@PBS displayed good TC degradation activity in the photocatalysis-activated persulfate system. Ca. 97.5% TC ( $10 \text{ mg L}^{-1}$ ) could be degraded by SR-AOPs coupling light irradiation. In this work, the generation of various free radicals and non-free radical was also studied, and the degradation mechanism of the reaction was deeply explored. Furthermore, the degradation pathways of TC and the toxicity of major oxidation intermediates were proposed and assessed. In particular, the M- $\text{Fe}_3\text{O}_4$ -T@PBS in this work can accomplish effective recyclability, which can maintain high removal efficiencies and rates after 30 runs’ operation. In all, this work opens a promising prospect for the treatment of wastewater containing antibiotic in practical applications.

### Declaration of Competing Interest

The authors declare that they have no known competing financial interests or personal relationships that could have appeared to influence the work reported in this paper.

### Acknowledgments

This work was supported by National Natural Science Foundation of China (22176012, 51878023, 21806008), Beijing Natural Science Foundation (8202016), Great Wall Scholars Training Program Project of Beijing Municipality Universities (CIT&TCD20180323), Beijing Talent Project (2020A27), Science and Technology General Project of Beijing Municipal Education Commission (KM202110016010) and The Fundamental Research Funds for Beijing University of Civil Engineering and Architecture (X20147/X20141/X20135/X20146).

### Appendix A. Supplementary data

Supplementary data to this article can be found online at <https://doi.org/10.1016/j.cej.2021.131927>.

### References

- [1] V.-T. Nguyen, T.-B. Nguyen, C.-W. Chen, C.-M. Hung, T.-D.-H. Vo, J.-H. Chang, C.-D. Dong, Influence of pyrolysis temperature on polycyclic aromatic hydrocarbons production and tetracycline adsorption behavior of biochar derived from spent coffee ground, *Bioresour. Technol.* 284 (2019) 197–203.
- [2] L. Xu, H.e. Zhang, P. Xiong, Q. Zhu, C. Liao, G. Jiang, Occurrence, fate, and risk assessment of typical tetracycline antibiotics in the aquatic environment: a review, *Sci. Total Environ.* 753 (2021) 141975.
- [3] X. Liu, J.C. Steele, X.-Z. Meng, Usage, residue, and human health risk of antibiotics in Chinese aquaculture: a review, *Environ. Pollut.* 223 (2017) 161–169.
- [4] W. Zhou, Y. Han, Y. Tang, W. Shi, X. Du, S. Sun, G. Liu, Microplastics aggravate the bioaccumulation of two waterborne veterinary antibiotics in an edible bivalve species: potential mechanisms and implications for human health, *Environ. Sci. Technol.* 54 (2020) 8115–8122.

- [5] S.M. Zainab, M. Junaid, N. Xu, R.N. Malik, Antibiotics and antibiotic resistant genes (ARGs) in groundwater: a global review on dissemination, sources, interactions, environmental and human health risks, *Water Res.* 187 (2020), 116455.
- [6] F. Granados-Chinchilla, C. Rodríguez, Tetracyclines in food and feedstuffs: from regulation to analytical methods, bacterial resistance, and environmental and health implications, *J. Anal. Chem.* 2017 (2017), 131547.
- [7] E.A. Auerbach, E.E. Seyfried, K.D. McMahon, Tetracycline resistance genes in activated sludge wastewater treatment plants, *Water Res.* 41 (5) (2007) 1143–1151.
- [8] R. Daghrir, P. Drogui, Tetracycline antibiotics in the environment: a review, *Environ. Chem. Lett.* 11 (3) (2013) 209–227.
- [9] H. Peng, J. Cao, W. Xiong, Z. Yang, M. Jia, S. Sun, Z. Xu, Y. Zhang, H. Cai, Two-dimension N-doped nanoporous carbon from KCl thermal exfoliation of Zn-ZIF-L: efficient adsorption for tetracycline and optimizing of response surface model, *J. Hazard. Mater.* 402 (2021), 123498.
- [10] Q. Liao, H. Rong, M. Zhao, H. Luo, Z. Chu, R. Wang, Interaction between tetracycline and microorganisms during wastewater treatment: a review, *Sci. Total Environ.* 757 (2021) 143981, <https://doi.org/10.1016/j.scitotenv.2020.143981>.
- [11] S.-F. Pan, M.-P. Zhu, J.P. Chen, Z.-H. Yuan, L.-B. Zhong, Y.-M. Zheng, Separation of tetracycline from wastewater using forward osmosis process with thin film composite membrane—Implications for antibiotics recovery, *Sep. Purif. Technol.* 153 (2015) 76–83.
- [12] Y. Liu, G. Gao, C.D. Vecitis, Prospects of an electroactive carbon nanotube membrane toward environmental applications, *Acc. Chem. Res.* 53 (12) (2020) 2892–2902.
- [13] A. Tufail, W.E. Price, F.I. Hai, A critical review on advanced oxidation processes for the removal of trace organic contaminants: a voyage from individual to integrated processes, *Chemosphere* 260 (2020), 127460.
- [14] Y. Yang, X. Li, C. Zhou, W. Xiong, G. Zeng, D. Huang, C. Zhang, W. Wang, B. Song, X. Tang, X. Li, H. Guo, Recent advances in application of graphitic carbon nitride-based catalysts for degrading organic contaminants in water through advanced oxidation processes beyond photocatalysis: a critical review, *Water Res.* 184 (2020) 116200.
- [15] D. Zhi, J. Wang, Y. Zhou, Z. Luo, Y. Sun, Z. Wan, L. Luo, D.C. Tsang, D. Dionysiou, Development of ozonation and reactive electrochemical membrane coupled process: enhanced tetracycline mineralization and toxicity reduction, *Chem. Eng. J.* 383 (2020), 123149.
- [16] X. Ao, W. Sun, S. Li, C. Yang, C. Li, Z. Lu, Degradation of tetracycline by medium pressure UV-activated peroxymonosulfate process: influencing factors, degradation pathways, and toxicity evaluation, *Chem. Eng. J.* 361 (2019) 1053–1062.
- [17] Y. Su, X. Wang, S. Dong, S. Fu, D. Zhou, B.E. Rittmann, Towards a simultaneous combination of ozonation and biodegradation for enhancing tetracycline decomposition and toxicity elimination, *Bioresour. Technol.* 304 (2020), 123009.
- [18] S. Giannakis, K.-Y.-A. Lin, F. Ghanbari, A review of the recent advances on the treatment of industrial wastewaters by Sulfate Radical-based Advanced Oxidation Processes (SR-AOPs), *Chem. Eng. J.* 406 (2020), 127083.
- [19] Y. Yang, P. Zhang, K. Hu, X. Duan, Y. Ren, H. Sun, S. Wang, Sustainable redox processes induced by peroxymonosulfate and metal doping on amorphous manganese dioxide for nonradical degradation of water contaminants, *Appl. Catal. B* 286 (2021), 119903.
- [20] D. Yuan, C. Zhang, S. Tang, Z. Wang, Q. Sun, X. Zhang, T. Jiao, Q. Zhang, Ferric ion-ascorbic acid complex catalyzed calcium peroxide for organic wastewater treatment: optimized by response surface method, *Chin. Chem. Lett.* (2021), <https://doi.org/10.1016/j.ccl.2021.04.050>.
- [21] X. Du, M. Zhou, Strategies to enhance catalytic performance of metal-organic frameworks in sulfate radical-based advanced oxidation processes for organic pollutants removal, *Chem. Eng. J.* 403 (2020), 126346.
- [22] J. Yan, M. Lei, L. Zhu, M.N. Anjum, J. Zou, H. Tang, Degradation of sulfamonomethoxine with Fe<sub>3</sub>O<sub>4</sub> magnetic nanoparticles as heterogeneous activator of persulfate, *J. Hazard. Mater.* 186 (2-3) (2011) 1398–1404.
- [23] S. Wu, D. Yang, Y. Zhou, H. Zhou, S. Ai, Y. Yang, Z. Wan, L. Luo, L. Tang, D. C. Tsang, Simultaneous degradation of p-arsanilic acid and inorganic arsenic removal using M-rGO/PS Fenton-like system under neutral conditions, *J. Hazard. Mater.* 399 (2020), 123032.
- [24] B. Roshani, N. Karpel vel Leitner, The influence of persulfate addition for the degradation of micropollutants by ionizing radiation, *Chem. Eng. J.* 168 (2) (2011) 784–789.
- [25] C. Tan, N. Gao, Y. Deng, N.a. An, J. Deng, Heat-activated persulfate oxidation of diuron in water, *Chem. Eng. J.* 203 (2012) 294–300.
- [26] H. Luo, Q. Lin, X. Zhang, Z. Huang, S. Liu, J. Jiang, R. Xiao, X. Liao, New insights into the formation and transformation of active species in nZVI/BC activated persulfate in alkaline solutions, *Chem. Eng. J.* 359 (2019) 1215–1223.
- [27] Z. Wei, F.A. Villamena, L.K. Weavers, Kinetics and mechanism of ultrasonic activation of persulfate: an in situ EPR spin trapping study, *Environ. Sci. Technol.* 51 (6) (2017) 3410–3417.
- [28] W. Ren, G. Nie, P. Zhou, H. Zhang, X. Duan, S. Wang, The intrinsic nature of persulfate activation and N-doping in carbocatalysis, *Environ. Sci. Technol.* 54 (10) (2020) 6438–6447.
- [29] J. Yang, M. Zhu, D.D. Dionysiou, What is the role of light in persulfate-based advanced oxidation for water treatment? *Water Res.* 189 (2020), 116627.
- [30] X.-H. Yi, C.-C. Wang, Elimination of emerging organic contaminants in wastewater by advanced oxidation process over iron-based MOFs and their composites, *Prog. Chem.* 33 (2021) 471.
- [31] C.-C. Wang, X. Wang, W. Liu, The synthesis strategies and photocatalytic performances of TiO<sub>2</sub>/MOFs composites: a state-of-the-art review, *Chem. Eng. J.* 391 (2019), 123601.
- [32] K. Yue, X. Zhang, S. Jiang, J. Chen, Y. Yang, F. Bi, Y. Wang, Recent advances in strategies to modify MIL-125 (Ti) and its environmental applications, *J. Mol. Liq.* 335 (2021), 116108.
- [33] M. Jia, Z. Yang, H. Xu, P. Song, W. Xiong, J. Cao, Y. Zhang, Y. Xiang, J. Hu, C. Zhou, Integrating N and F co-doped TiO<sub>2</sub> nanotubes with ZIF-8 as photoelectrode for enhanced photo-electrocatalytic degradation of sulfamethazine, *Chem. Eng. J.* 388 (2020), 124388.
- [34] Y.-H. Li, X.-H. Yi, Y.-X. Li, C.-C. Wang, P. Wang, C. Zhao, W. Zheng, Robust Cr (VI) reduction over hydroxyl modified UiO-66 photocatalyst constructed from mixed ligands: Performances and mechanism insight with or without tartaric acid, *Environ. Res.* 201 (2021), 111596.
- [35] N. Ojha, S. Kumar, Tri-phase photocatalysis for CO<sub>2</sub> reduction and N<sub>2</sub> fixation with efficient electron transfer on a hydrophilic surface of transition-metal-doped MIL-88A (Fe), *Appl. Catal. B* 292 (2021), 120166.
- [36] V.P. Viswanathan, K. Divya, D.P. Dubal, N.N. Adarsh, S. Mathew, Ag/AgCl@ MIL-88A (Fe) heterojunction ternary composites: towards the photocatalytic degradation of organic pollutants, *Dalton Trans.* 50 (2021) 2891–2902.
- [37] Y. Yang, W. Ji, X. Li, Z. Zheng, F. Bi, M. Yang, J. Xu, X. Zhang, Insights into the degradation mechanism of perfluorooctanoic acid under visible-light irradiation through fabricating flower-shaped Bi<sub>5</sub>O<sub>7</sub>/ZnO nn heterojunction microspheres, *Chem. Eng. J.* 420 (2021), 129934.
- [38] C. Zhao, Y. Li, H. Chu, X. Pan, L. Ling, P. Wang, H. Fu, C.-C. Wang, Z. Wang, Construction of direct Z-scheme Bi<sub>5</sub>O<sub>7</sub>/UiO-66-NH<sub>2</sub> heterojunction photocatalysts for enhanced degradation of ciprofloxacin: mechanism insight, pathway analysis and toxicity evaluation, *J. Hazard. Mater.* 419 (2021), 126466.
- [39] J.-W. Wang, F.-G. Qiu, P. Wang, C. Ge, C.-C. Wang, Boosted bisphenol A and Cr (VI) cleanup over Z-scheme WO<sub>3</sub>/MIL-100 (Fe) composites under visible light, *J. Clean. Prod.* 279 (2021), 123408.
- [40] X.-H. Yi, H. Ji, C.-C. Wang, Y. Li, Y.-H. Li, C. Zhao, A. Wang, H. Fu, P. Wang, X. Zhao, Photocatalysis-activated SR-AOP over PDINH/MIL-88A (Fe) composites for boosted chloroquine phosphate degradation: performance, mechanism, pathway and DFT calculations, *Appl. Catal. B* 293 (2021), 120229.
- [41] D. Huang, G. Wang, M. Cheng, G. Zhang, S. Chen, Y. Liu, Z. Li, W. Xue, L. Lei, R. Xiao, Optimal preparation of catalytic Metal-organic framework derivatives and their efficient application in advanced oxidation processes, *Chem. Eng. J.* 421 (2021), 127817.
- [42] Y.-X. Li, Y.-C. Han, C.-C. Wang, Fabrication strategies and Cr (VI) elimination activities of the MOF-derivatives and their composites, *Chem. Eng. J.* 405 (2021), 126648.
- [43] X. Zhang, F. Bi, Z. Zhu, Y. Yang, S. Zhao, J. Chen, X. Lv, Y. Wang, J. Xu, N. Liu, The promoting effect of H<sub>2</sub>O on rod-like MnCeOx derived from MOFs for toluene oxidation: a combined experimental and theoretical investigation, *Appl. Catal. B* 297 (2021), 120393.
- [44] D. Han, J. Wan, Y. Ma, Y. Wang, Y. Li, D. Li, Z. Guan, New insights into the role of organic chelating agents in Fe (II) activated persulfate processes, *Chem. Eng. J.* 269 (2015) 425–433.
- [45] H. Zhou, J. Peng, J. Li, J. You, L. Lai, R. Liu, Z. Ao, G. Yao, B. Lai, Metal-free black-red phosphorus as an efficient heterogeneous reductant to boost Fe<sup>3+</sup>/Fe<sup>2+</sup> cycle for peroxymonosulfate activation, *Water Res.* 188 (2021), 116529.
- [46] Y. Wang, C.-Y. Gao, Y.-Z. Zhang, M.K. Leung, J.-W. Liu, S.-Z. Huang, G.-L. Liu, J.-F. Li, H.-Z. Zhao, Bimetal-organic framework derived CoFe/NC porous hybrid nanorods as high-performance persulfate activators for bisphenol A degradation, *Chem. Eng. J.* 421 (2021), 127800.
- [47] C. Liu, Y. Wang, Y. Zhang, R. Li, W. Meng, Z. Song, F. Qi, B. Xu, W. Chu, D. Yuan, Enhancement of Fe@ porous carbon to be an efficient mediator for peroxymonosulfate activation for oxidation of organic contaminants: incorporation NH<sub>2</sub>-group into structure of its MOF precursor, *Chem. Eng. J.* 354 (2018) 835–848.
- [48] X. Li, F. Liao, L. Ye, L. Yeh, Controlled pyrolysis of MIL-88A to prepare iron/carbon composites for synergistic persulfate oxidation of phenol: catalytic performance and mechanism, *J. Hazard. Mater.* 398 (2020) 122938.
- [49] Z. Shi, Y. Zhang, X. Shen, G. Duoerkun, B. Zhu, L. Zhang, M. Li, Z. Chen, Fabrication of g-C<sub>3</sub>N<sub>4</sub>/BiOBr heterojunctions on carbon fibers as weavable photocatalyst for degrading tetracycline hydrochloride under visible light, *Chem. Eng. J.* 386 (2020), 124010.
- [50] S.-K. Park, J.K. Kim, Y.C. Kang, Electrochemical properties of uniquely structured Fe<sub>2</sub>O<sub>3</sub> and FeSe<sub>2</sub>/graphitic-carbon microrods synthesized by applying a metal-organic framework, *Chem. Eng. J.* 334 (2018) 2440–2449.
- [51] R. Yang, Y. Wang, Q. Deng, P. Hui, Z. Luo, Y. Yan, L. Wang, Metal-organic framework derived Fe<sub>3</sub>O<sub>4</sub>/C/rGO composite as an anode material in lithium-ion batteries, *Ionics* 27 (8) (2021) 3281–3289.
- [52] M. Tong, F. Liu, Q. Dong, Z. Ma, W. Liu, Magnetic Fe<sub>3</sub>O<sub>4</sub>-deposited flower-like MoS<sub>2</sub> nanocomposites for the Fenton-like Escherichia coli disinfection and diclofenac degradation, *J. Hazard. Mater.* 385 (2020), 121604.
- [53] K. Yang, H. Zhong, Z.-P. Cheng, X.-R. Li, A.-R. Zhang, T.-I. Li, Y.-J. Zhang, G.-Q. Liu, H.-Y. Qian, Magnetic Fe<sub>3</sub>O<sub>4</sub> stacked sphere-like nanocomposite and its application as platform for H<sub>2</sub>O<sub>2</sub> sensing, *J. Electroanal. Chem.* 814 (2018) 1–6.
- [54] D.D. Suppiah, S.B. Abd Hamid, One step facile synthesis of ferromagnetic magnetite nanoparticles, *J. Magn. Magn. Mater.* 414 (2016) 204–208.
- [55] D. Malwal, P. Gopinath, Silica stabilized magnetic-chitosan beads for removal of arsenic from water, *Colloids Interface Sci. Commun.* 19 (2017) 14–19.
- [56] H. Guo, H. Wang, N. Zhang, J. Li, J. Liu, A. Alsaedi, T. Hayat, Y. Li, Y. Sun, Modeling and EXAFS investigation of U (VI) sequestration on Fe<sub>3</sub>O<sub>4</sub>/PCMs composites, *Chem. Eng. J.* 369 (2019) 736–744.

- [57] S. Tang, M. Zhao, D. Yuan, X. Li, Z. Wang, X. Zhang, T. Jiao, J. Ke, Fe<sub>3</sub>O<sub>4</sub> nanoparticles three-dimensional electro-peroxydisulfate for improving tetracycline degradation, *Chemosphere* 268 (2021), 129315.
- [58] J. Lu, Y. Zhou, Y. Zhou, Efficiently activate peroxymonosulfate by Fe<sub>3</sub>O<sub>4</sub>@MoS<sub>2</sub> for rapid degradation of sulfonamides, *Chem. Eng. J.* 422 (2021), 130126.
- [59] B. Zhu, D. Song, T. Jia, W. Sun, D. Wang, L. Wang, J. Guo, L. Jin, L. Zhang, H. Tao, Effective visible light-driven photocatalytic degradation of ciprofloxacin over flower-like Fe<sub>3</sub>O<sub>4</sub>/Bi<sub>2</sub>WO<sub>6</sub> composites, *ACS Omega* 6 (2) (2021) 1647–1656.
- [60] J.-Y. Pu, J.-Q. Wan, Y. Wang, Y.-W. Ma, Different Co-based MOFs templated synthesis of Co<sub>3</sub>O<sub>4</sub> nanoparticles to degrade RhB by activation of oxone, *RSC Adv.* 6 (94) (2016) 91791–91797.
- [61] H. Li, J. Wan, Y. Ma, Y. Wang, M. Huang, Influence of particle size of zero-valent iron and dissolved silica on the reactivity of activated persulfate for degradation of acid orange 7, *Chem. Eng. J.* 237 (2014) 487–496.
- [62] H. Li, J. Wan, Y. Ma, M. Huang, Y. Wang, Y. Chen, New insights into the role of zero-valent iron surface oxidation layers in persulfate oxidation of dibutyl phthalate solutions, *Chem. Eng. J.* 250 (2014) 137–147.
- [63] Q. Zhang, L. Jiang, J. Wang, Y. Zhu, Y. Pu, W. Dai, Photocatalytic degradation of tetracycline antibiotics using three-dimensional network structure perylene diimide supramolecular organic photocatalyst under visible-light irradiation, *Appl. Catal. B* 277 (2020), 119122.
- [64] T. Zhang, Y. Liu, Y. Rao, X. Li, D. Yuan, S. Tang, Q. Zhao, Enhanced photocatalytic activity of TiO<sub>2</sub> with acetylene black and persulfate for degradation of tetracycline hydrochloride under visible light, *Chem. Eng. J.* 384 (2020), 123350.
- [65] C. Zhao, J. Wang, X. Chen, Z. Wang, H. Ji, L. Chen, W. Liu, C.-C. Wang, Bifunctional Bi<sub>12</sub>O<sub>17</sub>Cl<sub>2</sub>/ML-100 (Fe) composites toward photocatalytic Cr (VI) sequestration and activation of persulfate for bisphenol A degradation, *Sci. Total Environ.* 752 (2021), 141901.
- [66] G. Boczkaj, A. Fernandes, Wastewater treatment by means of advanced oxidation processes at basic pH conditions: a review, *Chem. Eng. J.* 320 (2017) 608–633.
- [67] Q. Wang, P. Li, Z. Zhang, C. Jiang, K. Zuoqiao, J. Liu, Y. Wang, Kinetics and mechanism insights into the photodegradation of tetracycline hydrochloride and ofloxacin mixed antibiotics with the flower-like BiOCl/TiO<sub>2</sub> heterojunction, *J. Photochem. Photobiol. A* 378 (2019) 114–124.
- [68] J. Ma, Y. Yang, X. Jiang, Z. Xie, X. Li, C. Chen, H. Chen, Impacts of inorganic anions and natural organic matter on thermally activated persulfate oxidation of BTEX in water, *Chemosphere* 190 (2018) 296–306.
- [69] M. Peters, Q. Guo, H. Strauss, R. Wei, S. Li, F. Yue, Contamination patterns in river water from rural Beijing: a hydrochemical and multiple stable isotope study, *Sci. Total Environ.* 654 (2019) 226–236.
- [70] M. Peters, Q. Guo, H. Strauss, R. Wei, S. Li, F. Yue, Seasonal effects on contamination characteristics of tap water from rural Beijing: a multiple isotope approach, *J. Hydrol.* 588 (2020), 125037.
- [71] L. Yang, J. He, Y. Liu, J. Wang, L. Jiang, G. Wang, Characteristics of change in water quality along reclaimed water intake area of the Chaobai River in Beijing, *China, J. Environ. Sci. (China)* 50 (2016) 93–102.
- [72] C. Qi, X. Liu, Y. Li, C. Lin, J. Ma, X. Li, H. Zhang, Enhanced degradation of organic contaminants in water by peroxydisulfate coupled with bisulfite, *J. Hazard. Mater.* 328 (2017) 98–107.
- [73] J. Wang, S. Wang, Effect of inorganic anions on the performance of advanced oxidation processes for degradation of organic contaminants, *Chem. Eng. J.* 411 (2021), 128392.
- [74] Y.-X. Li, C.-C. Wang, H. Fu, P. Wang, Marigold-flower-like TiO<sub>2</sub>/MIL-125 core-shell composite for enhanced photocatalytic Cr (VI) reduction, *J. Environ. Chem. Eng.* 9 (2021), 105451.
- [75] L. Wu, C.-C. Wang, H.-Y. Chu, X.-H. Yi, P. Wang, C. Zhao, H. Fu, Bisphenol A cleanup over ML-100 (Fe)/CoS composites: Pivotal role of Fe-S bond in regenerating Fe<sup>2+</sup> ions for boosted degradation performance, *Chemosphere* 280 (2021), 130659.
- [76] D. Yuan, M. Sun, S. Tang, Y. Zhang, Z. Wang, J. Qi, Y. Rao, Q. Zhang, All-solid-state BiVO<sub>4</sub>/ZnIn<sub>2</sub>S<sub>4</sub> Z-scheme composite with efficient charge separations for improved visible light photocatalytic organics degradation, *Chin. Chem. Lett.* 31 (2) (2020) 547–550.
- [77] T. Ge, Z. Jiang, L. Shen, J. Li, Z. Lu, Y. Zhang, F. Wang, Synthesis and application of Fe<sub>3</sub>O<sub>4</sub>/FeWO<sub>4</sub> composite as an efficient and magnetically recoverable visible light-driven photocatalyst for the reduction of Cr(VI), *Sep. Purif. Technol.* 263 (2021), 118401.
- [78] Q. Liu, L. Zhou, L. Liu, J. Li, S. Wang, H. Znad, S. Liu, Magnetic ZnO@Fe<sub>3</sub>O<sub>4</sub> composite for self-generated H<sub>2</sub>O<sub>2</sub> toward photo-Fenton-like oxidation of nitrophenol, *Compos. B. Eng.* 200 (2020), 108345.
- [79] J. Liu, X. Zhang, Q. Zhong, J. Li, H. Wu, B. Zhang, L. Jin, H.B. Tao, B. Liu, Electrostatic self-assembly of a AgI/Bi<sub>2</sub>Ga<sub>2</sub>O<sub>9</sub> p-n junction photocatalyst for boosting superoxide radical generation, *J. Mater. Chem. A* 8 (2020) 4083–4090.
- [80] J. Qu, D. Chen, N. Li, Q. Xu, H. Li, J. He, J. Lu, Coral-inspired nanoscale design of porous SnS<sub>2</sub> for photocatalytic reduction and removal of aqueous Cr (VI), *Appl. Catal. B* 207 (2017) 404–411.
- [81] H. Li, S. Sun, H. Ji, W. Liu, Z. Shen, Enhanced activation of molecular oxygen and degradation of tetracycline over Cu-S<sub>4</sub> atomic clusters, *Appl. Catal. B* 272 (2020), 118966.
- [82] G. Fan, X. Liu, X. Li, C. Lin, M. He, W. Ouyang, Mechanochemical treatment with CaO-activated PDS of HCB contaminated soils, *Chemosphere* 257 (2020), 127207.
- [83] D. Guo, Y. Liu, H. Ji, C.-C. Wang, B. Chen, C. Shen, F. Li, Y. Wang, P. Lu, W. Liu, Silicate-enhanced heterogeneous flow-through Electro-Fenton system using iron oxides under Nanoconfinement, *Environ. Sci. Technol.* 55 (6) (2021) 4045–4053.
- [84] Y. Chen, R. Yin, L. Zeng, W. Guo, M. Zhu, Insight into the effects of hydroxyl groups on the rates and pathways of tetracycline antibiotics degradation in the carbon black activated peroxydisulfate oxidation process, *J. Hazard. Mater.* 412 (2021), 125256.
- [85] W. Li, Y. Li, D. Zhang, Y. Lan, J. Guo, CuO-Co<sub>3</sub>O<sub>4</sub>@CeO<sub>2</sub> as a heterogeneous catalyst for efficient degradation of 2,4-dichlorophenoxyacetic acid by peroxymonosulfate, *J. Hazard. Mater.* 381 (2020), 121209.
- [86] M. Xu, J. Deng, A. Cai, X. Ma, J. Li, Q. Li, X. Li, Comparison of UVC and UVC/persulfate processes for tetracycline removal in water, *Chem. Eng. J.* 384 (2020), 123320.
- [87] Y. Wang, C. Zhou, J. Wu, J. Niu, Insights into the electrochemical degradation of sulfamethoxazole and its metabolite by Ti/SnO<sub>2</sub>-Sb/Er-PbO<sub>2</sub> anode, *Chin. Chem. Lett.* 31 (10) (2020) 2673–2677.